frontiers in Neuroscience

ORIGINAL RESEARCH
published: 15 May 2019
doi: 10.3389/fnins.2019.00488

Tau Inclusions in Alzheimer's, Chronic Traumatic Encephalopathy and Pick's Disease. A Speculation on How Differences in Backbone Polarization Underlie Divergent Pathways of Tau Aggregation

Andrzej Stanisław Cieplak[1,2,3]*

[1] Department of Chemistry, Bilkent University, Ankara, Turkey, [2] Department of Chemistry, Yale University, New Haven, CT, United States, [3] Department of Chemistry, Brandeis University, Waltham, MA, United States

OPEN ACCESS

Edited by:
Masato Hasegawa, Tokyo Metropolitan Institute of Medical Science, Japan

Reviewed by:
Yoshiki Yamaguchi, RIKEN Brain Science Institute (BSI), Japan
Fuyuki Kametani, Tokyo Metropolitan Institute of Medical Science, Japan

***Correspondence:**
Andrzej Stanisław Cieplak
cieplak@gmail.com

Specialty section:
This article was submitted to Neurodegeneration, a section of the journal Frontiers in Neuroscience

Received: *25 January 2019*
Accepted: *29 April 2019*
Published: *15 May 2019*

Citation:
Cieplak AS (2019) Tau Inclusions in Alzheimer's, Chronic Traumatic Encephalopathy and Pick's Disease. A Speculation on How Differences in Backbone Polarization Underlie Divergent Pathways of Tau Aggregation. Front. Neurosci. 13:488. doi: 10.3389/fnins.2019.00488

Tau-related dementias appear to involve specific to each disease aggregation pathways and morphologies of filamentous tau assemblies. To understand etiology of these differences, here we elucidate molecular mechanism of formation of tau PHFs based on the PMO theory of misfolding and aggregation of pleiomorphic proteins associated with neurodegenerative diseases. In this model, fibrillization of tau is initiated by the coupled binding and folding of the MTB domains that yields antiparallel homodimers, in analogy to folding of split inteins. The free energy of binding is minimized when the antiparallel alignment brings about backbone-backbone H-bonding between the MTBD segments of similar "strand" propensities. To assess these propensities, a function of the NMR shielding tensors of the C^{α} atoms is introduced as the *folding potential* function FP_i; the C^{α} tensors are obtained by the quantum mechanical modeling of protein secondary structure (GIAO//B3LYP/D95**). The calculated FP_i plots show that the "strand" propensities of the MBTD segments, and hence the homodimer's register, can be affected by the relatively small changes in the environment's pH, as a result of protonation of MBTD's conserved histidines. The assembly of the antiparallel tau dimers into granular aggregates and their subsequent conversion into the parallel cross-β structure of paired helical filaments is expected to follow the same path as the previously described fibrillization of Aβ. Consequently, the core structure of the nascent tau fibril is determined by the register of the tau homodimer. This model accounts for the reported differences in (i) fibril-core structure of *in vivo* and *in vitro* filaments, (ii) cross-seeding of isoforms, (iii) effects of reducing/non-reducing conditions, (iv) effects of PHF6 mutations, and (v) homologs' aggregation properties. The proposed model also

suggests that in contrast to Alzheimer's and chronic traumatic encephalopathy disease, the assembly of tau prions in Pick's disease would be facilitated by a moderate drop in pH that accompanies e.g., transit in the endosomal system, inflammation response or an ischemic injury.

Keywords: intrinsically disordered proteins, polypeptide backbone, tau aggregation, Alzheimer's disease, Pick's disease, chronic traumatic encephalopathy, aberrant proteostasis, cross-seeding barriers

INTRODUCTION

Aberrant proteostasis appears to be at the core of a host of neurodegenerative and mental disorders, from Alzheimer's to schizophrenia (Bradshaw and Korth, 2018). Thus, a thorough understanding of what makes some proteins prone to aberrant folding may be necessary to meet one of the most pressing challenges of modern times. Unfortunately, our current understanding of protein folding and misfolding is limited for want of a physicochemical theory of protein secondary and tertiary structure (Baldwin and Rose, 1999). Recognizing these limitations, an attempt was recently made to construct such a theory, using the PMO theory-informed approach and focusing on the electronic configuration and hyperconjugation of the peptide amide bonds (Cieplak, 2017). To capture the effect of polarization of peptide linkages on the conformational and H-bonding propensity of the polypeptide backbone, a function of the NMR shielding tensors of the C^{α} atoms was introduced as the *folding potential* function FP_i. The FP_i function proved to be an effective tool to investigate conformational behavior of the intrinsically disordered and pleiomorphic proteins, revealing a common pattern of backbone density distribution in the amyloidogenic regions of several highly pleiomorphic proteins associated with neurodegenerative diseases: amyloid beta Aβ, tau, α-synuclein αS, and mammalian prions PrP^{C}. A common molecular model of aggregation of these proteins was consequently proposed (Cieplak, 2017).

Here we apply this model to address the complexities of polymerization of tau. There is a growing recognition of the role of tau in a wide range of brain proteinopathies and consequently a growing interest in the structure and the mechanism of self-replication and cell-to-cell transmission of tau prions (Bemporad and Chiti, 2012; del Carmen Cárdenas-Aguayo et al., 2014; Hasegawa, 2016; Wang and Mandelkow, 2016; Goedert and Spillantini, 2017; Goedert et al., 2017; Guo et al., 2017; Nizynski et al., 2017; Ayers et al., 2018; Demaegd et al., 2018; Gao et al., 2018; Sebastián-Serrano et al., 2018). Fibrillization of tau appears broadly similar to the fibrillization of Aβ and αS but relatively few details are available concerning its early stages and the nature of low-order oligomers (Pavlova et al., 2016; Eschmann et al., 2017; Huang et al., 2018). It is believed that fibrillization is initiated by the dimerization of tau (Friedhoff et al., 1998; Sugino et al., 2009; Kumar et al., 2014) which, it is now reported, may involve a host of seeding-competent monomer conformers that encode strains of tau prions (Mirbaha et al., 2018; Sharma et al., 2018). The dimerization is followed by the assembly of dimers into granular aggregates (Maeda et al., 2007; Ren and Sahara, 2013; Karikari et al., 2019) and subsequent conversion of these aggregates into filaments. The process apparently involves divergent paths of dimerization and oligomerization since the tau-related dementias are found to involve specific to each disease aggregation pathways and morphologies of filamentous tau assemblies (Sanders et al., 2014; Dujardin et al., 2018). Thus, the cryo-EM investigation has recently shown that paired helical filaments of tau isolated from the brains of Pick's, Alzheimer's and chronic traumatic encephalopathy (CTE) patients are considerably different in their fibril-core structure (Fitzpatrick et al., 2017; Falcon et al., 2018, 2019), while the *in vitro* heparin-induced fibrillization of the 4R isoform was found to yield a heterogenous mixture of several types of filaments, none in the Pick or Alzheimer fold (Fichou et al., 2018; Kjaergaard et al., 2018; Zhang et al., 2018). The filamentous deposits of tau can also be different in terms of the isoform composition which turns out to be specific to each disease as well. For instance, Pick's filaments contain only 3R isoforms, progressive supranuclear palsy filaments only 4R isoforms, while Alzheimer's filaments contain both 3R and 4R isoforms. The reasons for the presence or absence of barriers to cross-seeding of the 3R and 4R aggregates are not well-understood (Adams et al., 2010; Siddiqua et al., 2012; Yu et al., 2012; Kumar and Udgaonkar, 2018; Weismiller et al., 2018). In this paper, we describe molecular mechanism of fibrillization of tau which attributes the observed diversity of fibril morphology and asymmetric cross-seeding barriers to the variation in the pattern of backbone polarization and the concomitant variation in the conformational and H-bonding propensity of the amyloidogenic region of tau. The hypothesis is based on the investigation of the folding potential FP_i profiles for the MTB domains of tau and a few truncated tau constructs.

Computational Methods. A Protocol for Evaluation of Secondary Structure Propensity

The *folding potential* function FP_i is a function of the NMR shielding tensors of the C^{α} atoms, $\boldsymbol{\sigma}(C^{\alpha})^{Xaa}$, which were obtained by quantum mechanical modeling of protein secondary structure. The calculations were carried out using the oligopeptides $AcGXaaGGGNH_2$ and $AcGGGGGXaaNHMe$ as the models of the 3_{10}-helix and the hairpin with the type Ib reverse turn, respectively, at the B3LYP/D95** level of the theory [Gaussian 98, Revisions A.3, A.7, A11.2 (Frisch et al., 1998)], according to the protocol described previously in Cieplak (2017). The canonical and covalently modified residues Xaa (the L-amino acid series) of the hexapeptide hairpin and

the pentapeptide helix were systematically varied, taking into account side chain conformations (Kyte, 1995) and ionization state when appropriate, to yield the total of 141 congener structures. To compute the NMR shielding tensors using the atomic coordinates of the obtained structures, the B3LYP/D95** and GIAO (Gauge-Independent Atomic Orbital) methods were employed. The obtained $\boldsymbol{\sigma}(C^{\alpha})^{Xaa}$ tensor values are used to quantify the relationship between the density distribution and the conformational and H-bonding propensity of the polypeptide backbone via construction of *the folding potential* function FP_i. The folding constants σ^{Xaa} are first derived from the linear normalization of the mean $\boldsymbol{\sigma}(C^{\alpha})^{Xaa}$ tensor values to the scale where the σ^{Pro} constant for proline is −1 and the σ^{Gly} constant for glycine is 1, see **Table 1**. The folding potential at the residue i, FP_i, is then defined as the averaged sum of the mean μ_i and standard deviation σ_i of the constants σ^{Xaa} within the three-(i−1, i, i+1) and five-(i−2, i−1, i, i+1, i+2)-residue windows:

$$\begin{aligned} FP_i = \tfrac{1}{2}[&\mu_i(\sigma^{Xaa}{}_j; j = i-1, i, i+1) \\ &+\sigma_i(\sigma^{Xaa}{}_j; j = i-1, i, i+1) \\ &+\mu_i(\sigma^{Xaa}{}_j; j = i-2, i-1, i, i+1, i+2) \\ &+\sigma_i(\sigma^{Xaa}{}_j; j = i-2, i-1, i, i+1, i+2)] \end{aligned} \quad (1)$$

In addition, the slope of the folding potential at the residue i, $\Delta FP_{i-1\rightarrow i+1}$, is approximated by the difference of the folding potential at the residues $i-1$ and $i+1$:

$$\Delta FP_{i-1\rightarrow i+1} = FP_{i+1} - FP_{i-1} \quad (2)$$

While the folding potential function FP_i does not carry any information about the constraints introduced e.g., by the hydrophilic residues or by proline and obviously does not take into account any side chain-side chain interactions, the FP_i and FP_i vs. $\Delta FP_{i-1\rightarrow i+1}$ plots were found to identify essential elements of the secondary and tertiary structure of proteins when two theories of solutions, the Onsager theory of solute-solvent polarization (Onsager, 1936) and the Debye-Hückel theory of dilute solutions of strong electrolytes (Debye and Hückel, 1923), are taken into account. The main features of this model are summarized in **Figure 1** which comprises basic elements of the previously described theory (Cieplak, 2017).

Lastly, binary complexes of oligopeptides $(AcAAANHMe)_2$ and $(AcAAAAANHMe)_2$ were obtained by unconstrained optimization [as described above, at the B3LYP/6-31G* level of the theory, completed by the default convergence criteria of Gaussian98, cf. structures **6a**–**6d** and **7a**–**7b**/**8a**–**8c**, respectively, in Cieplak (2017)]. The individual strands in these complexes were found to optimize either to the C_5 or the C_{7eq} (2_7-ribbon) geometries, and their conformations are same in the antiparallel complexes ($C_5\uparrow C_5\downarrow$ or $C_{7eq}\uparrow C_{7eq}\downarrow$) and mixed in the parallel complexes ($C_{7eq}\uparrow C_5\uparrow$); *the antiparallel complexes with mixed strand conformations ($C_{7eq}\uparrow C_5\downarrow$) were found to be unstable in unconstrained optimizations*. These findings suggest that the preferred mode of assembly of the two-stranded β-sheets depends on charge polarization of the main chain as well. Accordingly, a mechanism of FP_i-directed molecular recognition in formation of β structure is presented in **Figure 2** which comprises main elements of the previously described theory (Cieplak, 2017).

TABLE 1 | Folding constants σ^{Xaa} of the canonical amino acids:[a,b] $\sigma^{Xaa} = \{[\boldsymbol{\sigma}(C^{\alpha})^{Xaa}(trans) + \boldsymbol{\sigma}(C^{\alpha})^{Xaa}(-gauche)] - [\boldsymbol{\sigma}(C^{\alpha})^{Gly} + \boldsymbol{\sigma}(C^{\alpha})^{Pro}]\}/[\boldsymbol{\sigma}(C^{\alpha})^{Gly} - \boldsymbol{\sigma}(C^{\alpha})^{Pro}]$.

Xaa	σ^{Xaa}	Xaa	σ^{Xaa}
A	0.1898	K	−0.0772
C	−0.4989	L	−0.0441
C[SMe]	−0.0403	M	−0.2143
D	0.1293	N	0.0296
D^-	−0.1087	P	−1
E	0.1889	Q	−0.2485
E^-	−0.4847	R	0.1683
F	−0.4289	S	−0.4700
G	1	T	−0.9066
H	−0.2917	V	−0.7703
H^+	0.2584	W	−0.2704
I	−0.7647	Y	−0.3981

[a] *Each tensor $\boldsymbol{\sigma}(C^{\alpha})$ is the average of the values obtained with two models of secondary structure, a hairpin (AcGGGGGXaaNHMe/Ib) and a helix (AcGXaaGGGNH$_2$/3_{10}), at the GIAO//B3LYP/D95** level of the theory. The mean values for the trans and –gauche conformers of the side chain about the C^{α}-C^{β} bond are taken when appropriate (Kyte, 1995).*

[b] *The σ^{Xaa} constants for some covalently modified amino acids are: Ser O^{γ}-PO_3^{-2} −1.1584, Ser O^{γ}-PO_3^{-1} approx. −0.6160, Met S(=O)$_2$−0.1101, Lys N^{ξ}-$COCH_3$−0.2518, Val C^{β}-CH_3−0.9993, Ala C^{β}-F_3−0.4258, Phe -F_5−0.0829, Leu C^{δ}-F_3/C^{δ}-F_3 0.0049, Ala C^{β}-CF_3 0.2713, Ala C^{β}-n-$CH_2CH_2CH_3$−0.2014, Thr C^{β}-$N^{\gamma}H_2$−0.8477, Gly C^{α}-C=N 0.8893, Gly C^{α}-C=NO 0.8500, Gly C^{α}-C=CH 0.6828.*

RESULTS AND DISCUSSION

(i) Electronic Configuration of the Polypeptide Backbone and the Antiparallel-to-Parallel β Structure Conversion as a Path to Paired Helical Filaments of Tau

According to the PMO theory of misfolding and aggregation of pleiomorphic proteins associated with common brain proteinopathies (Aβ, tau, αS, and PrP^C), polymerization of the intrinsically disordered amyloidogenic regions of these proteins depends on the distribution of backbone density which determines conformational and H-bonding propensity of the main chain (Cieplak, 2017). The relationship between the backbone polarization and conformational preferences of a given polypeptide chain is here quantified by the *folding potential* function FP_i, a function of the NMR shielding tensors of the C^{α} atoms, cf. Computational Methods. Thus, by taking into account the FP_i plots, and conformational properties of β sheets (Salemme, 1983; Branden and Tooze, 1999), one may arrive at a model of polymerization of those proteins. The resulting outline of the anticipated aggregation pathways is indeed shown in **Figure 3**.

The pathway which would lead to the assembly of tau PHFs is shown in **Figure 3C**. In the first stage of the process, the accessible segments of the microtubule binding domain MTBD form long antiparallel two-stranded β-sheets, by analogy

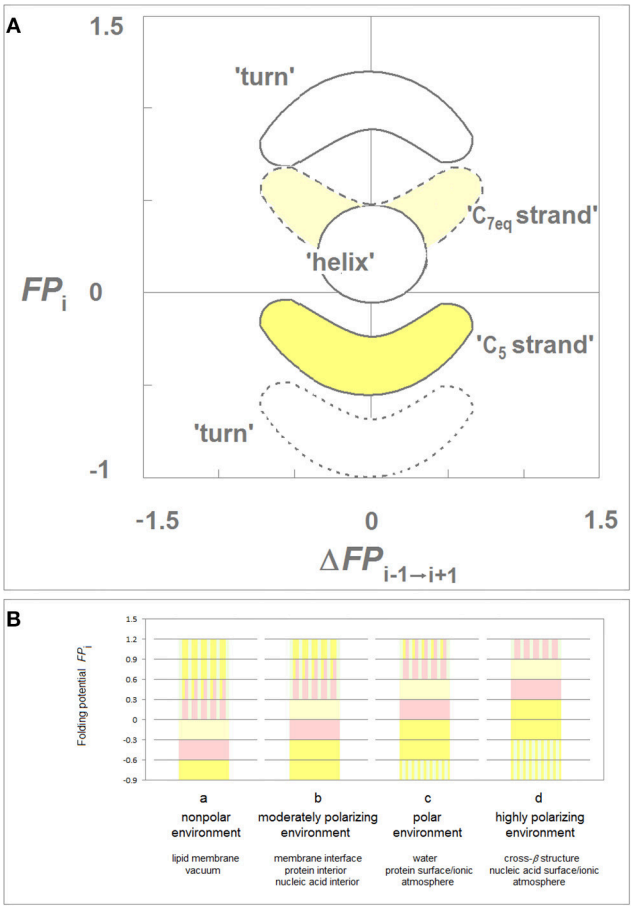

FIGURE 1 | Folding potential function FP_i as a probe of the three-dimensional structure of proteins. **(A)** Characteristic clusters of the data sets in the plots of FP_i vs. the "slope" of FP_i, $\Delta FP_{i-1\rightarrow i+1}$. The five clusters of data correspond to the three archetypal elements of the secondary structure: e.g., the presence of the archetypal "helix" will be marked by a compact cluster of data sets in the center of the plot. The ordinate of this cluster will vary since the optimal FP_i value for "helix" depends on the medium's capacity to polarize the protein, *vide infra*. Notice that "strand" and "turn" have each two avatars: (i) "C_5 strand" and "C_{7eq} strand," and (ii) "$FP_i >> 0$ turn" (defined here as the three- or five-residue segment that incorporates Gly in the center) and "$FP_i << 0$ turn." **(B)** Folding potential, medium properties and secondary structure preferences of the polypeptide backbone: (a) The FP_i values that ensure stability of the periodic secondary structure in a non-polar environment such as the lipid matrix of the bilayer membrane or vacuum: the optimal FP_i range for the α-helix is −0.6 to −0.3 and the optimal FP_i ranges for β structure is < -0.6 (C_5 strand) and −0.3 to 0 (C_{7eq} strand). The less polarized segments are malleable in a non-polar aprotic medium and may adopt helical (3_1-helix, PP_{II}-helix, α*-helix) folds while the least polarized segments of the polypeptide backbone, e.g., a sequence of consecutive "$FP_i >> 0$ turns," may adopt the extended (C^*_5 strand) folds depending on molecular embedding; (b) The FP_i values that ensure stability of the periodic secondary structure in a moderately polarizing environment such as the bilayer membrane interface, the interior of a soluble protein globule or the interior of the DNA duplex: the optimal FP_i range for the α-helix is −0.3 to 0 and the optimal FP_i ranges for β structure is < -0.3 (C_5 strand) and 0 to 0.3 (C_{7eq} strand); (c) The FP_i values that ensure stability of the periodic secondary structure in a polar medium such as the physiological 1:1 electrolyte solution: the range of the optimal FP_i values for the α-helix is now 0 to 0.3 while the somewhat less and more polarized segments are likely to form β-sheets. The most polarized segments are now

(Continued)

FIGURE 1 | likely to form "$FP_i << 0$ turns" or PP_{II}-helix. The sequence of consecutive "$FP_i >> 0$ turns" forms a random coil in an aqueous buffer unless it is stabilized by molecular embedding in helical (3_1-helix, PP_{II}-helix, α*-helix) or extended (C^*_5 strand) folds; (d) The FP_i values that ensure stability of the periodic secondary structure in the hypothetical highly polarizing environment such as the pre-organized ionic grid e.g., on the surface of a DNA or RNA strand (the sequence of consecutive "$FP_i >> 0$ turns" is likely to form here an α*-helix), or the microenvironment of the extended β structure of β solenoid or amyloid filament.

to the coupled binding and folding od split inteins (Shah et al., 2013; Eryilmaz et al., 2014); the assumed alignment mode is in accord with the results of quantum mechanical modeling of β structure (Cieplak, 2017). In the antiparallel alignment, the free energy of backbone-backbone H-bonding is minimized by binding the MTBD segments of *similar* "strand" propensities e.g., $C_5\uparrow C_5\downarrow$ or $C_{7eq}\uparrow C_{7eq}\downarrow$, cf. the model of molecular recognition in formation of β structure in **Figure 2**. Consequently, the register of the resulting antiparallel tau dimers is determined by the pattern of density distribution and concomitant conformational propensities of the polypeptide backbone of MTBD. The next stage involves head-to-tail association of the antiparallel homodimers into disk-shaped hexamers, and subsequent antiparallel-to-parallel conversion of β structure within the aggregates of such hexamers. This model was previously introduced to account for the rates and morphology of Aβ aggregation on diverse surfaces (Kowalewski and Holtzman, 1999; Qing et al., 2014; Gao et al., 2015), obligatory micelle-like and helical intermediates of Aβ fibrillization (Yong et al., 2002; Roychaudhuri et al., 2009; Vitalis and Caflisch, 2010; Wälti et al., 2015), SAXS data on Aβ dimers (Ryan et al., 2015), AFM data on the morphology of early oligomerization states of Aβ (Fu et al., 2015; Economou et al., 2016), cryo-EM data on the morphology of Aβ fibrils (Schmidt et al., 2015), and the catalysis of fibrillogenesis by the intercalating aromatic ions (Williams et al., 2005; Ladiwala et al., 2011; Bieschke et al., 2012). The presented here outline of divergent pathways of the fibrillization of tau is based on the assumption that this model applies to tau as well. Thus, the assembly of the antiparallel homodimers of tau into hexameric paranuclei—granular aggregates—and their subsequent conversion into the parallel cross-β structure leads to the formation of paired helical filaments. Importantly, the proposed mechanism of this conversion, see the detailed description below, preserves the homodimer's register in the core structure of the nascent fibril.

It follows that the repeat structure of the amyloidogenic MTB domain, marked by subtle differences in the electronic configuration of the repeat segments of the main chain, is likely to be one source of the observed diversity of tau-fibril morphology. The differences in conformational propensities and aggregation properties of the four repeats of the MTB domain of tau attracted considerable attention (Perez et al., 1996, 2007; von Bergen et al., 2000; Tokimasa et al., 2005; Naruto et al., 2010; Sogawa et al., 2012, 2014; Lathuillière et al., 2017; Macdonald et al., 2019). To gauge whether and how these differences are indeed related to the differences in backbone polarization, the folding potential

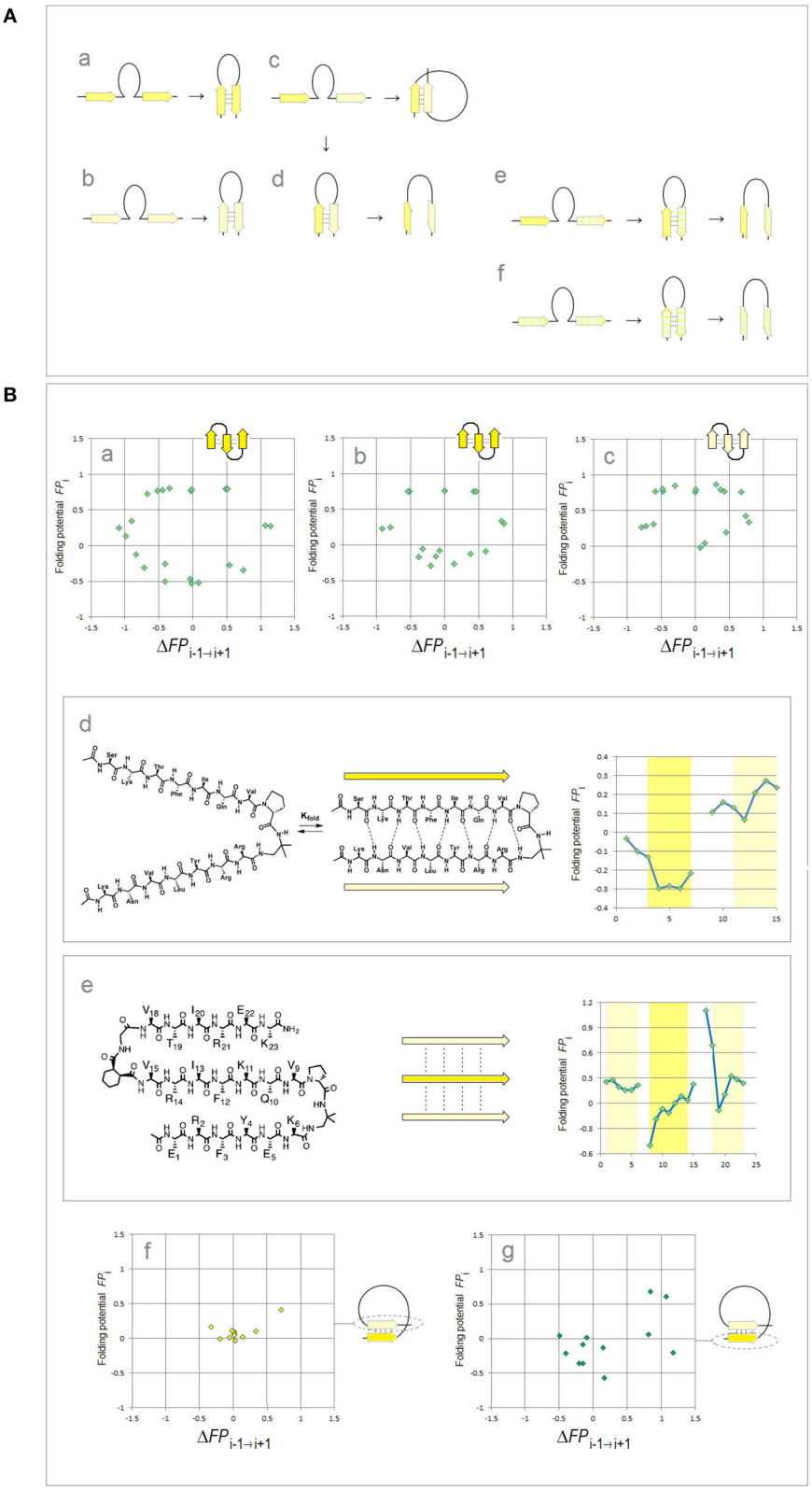

FIGURE 2 | Electronic configuration of the polypeptide backbone and molecular recognition in formation of β structure (Cieplak, 2017). **(A)** A model of alignment preferences in the complexes of the C_5 and C_{7eq} strands. The polypeptide segments comprising two consecutive strands form stable β-hairpins (antiparallel

(Continued)

FIGURE 2 | assembly) when the two strands are either (a) both highly polarized ($C_5\uparrow C_5\downarrow$) or (b) both moderately polarized ($C_{7eq}\uparrow C_{7eq}\downarrow$). In contrast, when one strand is highly polarized and the other is moderately polarized, these segments are expected to form (c) β-solenoid coils (parallel assembly, $C_{7eq}\uparrow C_5\uparrow$) or (d) unstable β-hairpins (antiparallel assembly $C_{7eq}\uparrow C_5\downarrow$) which are prone to convert into β-arches; similarly when one strand is highly polarized (C_5) and the other is least-polarized (C_5^*) (e), or both strands are least-polarized (f), the segment may form a hairpin which is also prone to convert into β-arch. Such conversions are particularly likely when the backbone H-bonding between the least-polarized strands is relatively weak and when the β-arch-like structure can be stabilized as a "steric zipper." **(B)** Electronic configuration of the polypeptide backbone in the autonomous β sheets. In the plots of FP_i vs. the "slope" of FP_i, $\Delta FP_{i-1\rightarrow i+1}$ (cf. **Figure 1**), the presence of the archetypal antiparallel "sheet" would be marked by a circular distribution of data sets that combines the "C_5 strand"/"$FP_i >> 0$ turn" or "C_{7eq} strand"/"$FP_i >> 0$ turn" clusters while the presence of the parallel "sheet" would be marked by a combination of the "C_5 strand" and "C_{7eq} strand" clusters. The *de novo* designed three-stranded antiparallel β-sheets (three-stranded β meanders) (de Alba et al., 1999; Griffiths-Jones and Searle, 2000; Lopez de la Paz et al., 2001) and two- and three-stranded parallel β-sheets (Fisk et al., 2006; Kung et al., 2015), and the two-stranded parallel β-sheets embedded in left-handed coils from the C-terminal domains of the penicillin binding protein PBP2x from *Streptococcus pneumoniae*, PDB ID 1k25, provide examples of the FP_i profiles which are consistent with this model: (a) KGEWTFVNGKYTVSINGKKITVSI, ∼50% in β structure, H_2O, pH 3, 25°C ($C_5\uparrow C_5\downarrow C_5\uparrow$-meander); (b) TWIQNGSTKWYQNGSTKIYT, 20–30% in β structure, H_2O, pH 3.25, 10°C ($C_5\uparrow C_5\downarrow C_5\uparrow$-meander); (c) RGWSLQNGKYTLNGKTMEGR, ∼35% in β structure, 10% D_2O/H_2O or D_2O, pH 5, 0–10°C ($C_{7eq}\uparrow C_{7eq}\downarrow C_{7eq}\uparrow$-meander); (d) $C_5\uparrow C_{7eq}\uparrow$-parallel sheet, cf. the FP_i plot. The C-termini of two strands are connected by the D-prolyl-1,1-dimethyl-1, 2-diaminoethane unit (diamine linker D-Pro-DADME), ∼64% "folding-core" residues (F5-V8 and R11-L14) in β structure at 10°C, 10% D_2O/H_2O, 100 mM sodium acetate buffer, pH 3.8; (e) $C_{7eq}\uparrow C_5\uparrow C_{7eq}\uparrow$-parallel sheet, cf. the FP_i plot. The C-termini of strands 1 and 2 are connected by the diamine D-Pro-DADME while the N-termini of strands 2 and 3 are connected by the diacid formed from (1*R*,2*S*)-cyclohexanedicarboxylic acid (CHDA) and Gly, 4°C, 10% D_2O/H_2O, 2.5 mM sodium [D_3]acetate buffer, pH 3.8; (f) the C_{7eq} strands from two $C_5\uparrow C_{7eq}\uparrow$-parallel sheets in the left-handed coils of PBP2x from *Streptococcus pneumoniae*, PDB ID 1k25; (g) the C_5 strands from two $C_5\uparrow C_{7eq}\uparrow$-parallel sheets in the left-handed coils of PBP2x, PDB ID 1k25.

FP_i is plotted against its "slope" $\Delta FP_{i-1\rightarrow i+1}$ separately for each repeat, see the FP_i vs. $\Delta FP_{i-1\rightarrow i+1}$ plots in **Figure 4**, where the side chains of the histidine residues of MTBD are either neutral (the side chain's imidazole ring is not protonated and $\sigma^{\mathrm{His}} = -0.2917$, **Table 1**), **Figure 4A**, or cationic (the side chain's imidazole ring is protonated and $\sigma^{\mathrm{His+}} = 0.2584$, **Table 1**), **Figure 4B**. Histidine pK_a's vary widely depending on burial within proteins (Edgcomb and Murphy, 2002; Miyagi and Nakazawa, 2008) but the pK_a values of the conserved histidines of MTBD are in the physiological range (Charafeddine et al., 2019). It seems safe to assume that depending on the buffer conditions commonly used in the fibrillization experiments (pH 6.0–7.6, anionic cofactors), no histidine side chains are protonated at the upper range of physiological pH, while some or all are likely to be protonated at a lower range of physiological pH. In either case, the scatterplots in **Figure 4** are dominated by the presence of multiple "$FP_i >> 0$ turns" and $\Delta FP_i \approx 0/\Delta FP_{i-1\rightarrow i+1} \approx 0$ clusters, indicating that MTBD lacks backbone elements which would have pronounced secondary structure propensity in aqueous buffers and can therefore adopt "helix" or "strand" fold in a less polar or more polar environment, respectively, cf. **Figure 1**. On the other hand, however, the "C_5 strand" propensity is also recognizable, most pronounced in the case of R3 but also in the case of R4, **Figure 4A**d, which makes R3 and R4 quite similar in terms of the FP_i profiles when histidines are not protonated. This similarity is lost upon protonation of histidine residues which makes R4 similar in terms of the FP_i profiles to R1 and R2, see **Figures 4B**a,b,d.

Extensive experimental studies point to R3 as crucial to the initiation of PHFs assembly and the following examination focuses on this repeat. The "barbell"-shaped FP_i profile of the V306-K321 segment of R3 shows, **Figure 5**, two hexapeptide motifs, V306-K311 (PHF6) and S316-K321, which have "C_5 strand" propensity in the aqueous buffers. The two hexapeptides are however connected by the string of residues P312-K317 with the helical FP_i profile and low FP_i so that in water this string can form neither a stable "turn" nor a stable "helix" and the entire segment remains disordered, **Figure 5B**. Once transferred, however, into a less polar environment e.g., protein interior, membrane interface or a non-polar solvent, the V306-K321 segment acquires "helix" propensity, **Figure 5A** cf. **Figure 1B**a, and it does indeed become helical in TFE solutions (Minoura et al., 2003; Tokimasa et al., 2005). On the other hand, in a more polarizing environment created by the backbone-backbone H-bonding (Sheridan et al., 1979; Cieplak and Sürmeli, 2004) in a two-stranded antiparallel β sheet formed in water, the entire V306-K321 segment acquires "C_5 strand" propensity cf. **Figure 5C**.

The ability to shift secondary structure preference upon the change of environment is essential to tau function but also underlies the "gain-of-structure" process, **Figures 5C,D**, that ultimately brings about the formation of paired helical filaments. As was mentioned earlier, the segments of MTBD first form long antiparallel two-stranded β-sheets. An example of such a homodimer which comprises three β-sheets $C_5^1\uparrow C_5^2\downarrow/C_5^*\uparrow C_5^*\downarrow/C_5^2\uparrow C_5^1\downarrow$ and is "appended" by the N-terminal "C_{7eq} strands," is shown in **Figure 5C**a. The head-to-tail aggregation of those dimers via domain swapping (here interlocking of the N-terminal strands to form the $C_{7eq}\uparrow C_{7eq}\downarrow$ β-sheets) yields disk-shaped hexameric polymerization nuclei. The circular conformation of these hexamers superposes the two-stranded antiparallel β-sheets on top of each other in the parallel alignment, see **Figure 5C**b.

As the polymerization nuclei subsequently assemble into granular aggregates, the V306-K321 segments are transferred from an aqueous environment into a less polar environment of the protein interior and become again disordered, **Figure 5D**. Consequently, the antiparallel β-sheets (β↑β'↓ and β"↑β"'↓) are destabilized and their strands can rotate about the axes to form the parallel β-sheets (β↑β"↑ and β'↑β"'↑) that extend the cross-β structure, see **Figure 5D**; the highly polarizing environment of the cross-β structure turns the V306-K321 segments back into the "C_5 strands." Thus, the nascent fibrils of tau comprise two parallel cross-β sheets (protofilaments) which are aligned in the antiparallel fashion, so that the 2-fold symmetry of the original homodimers is retained; the "appended" strands of the dimers

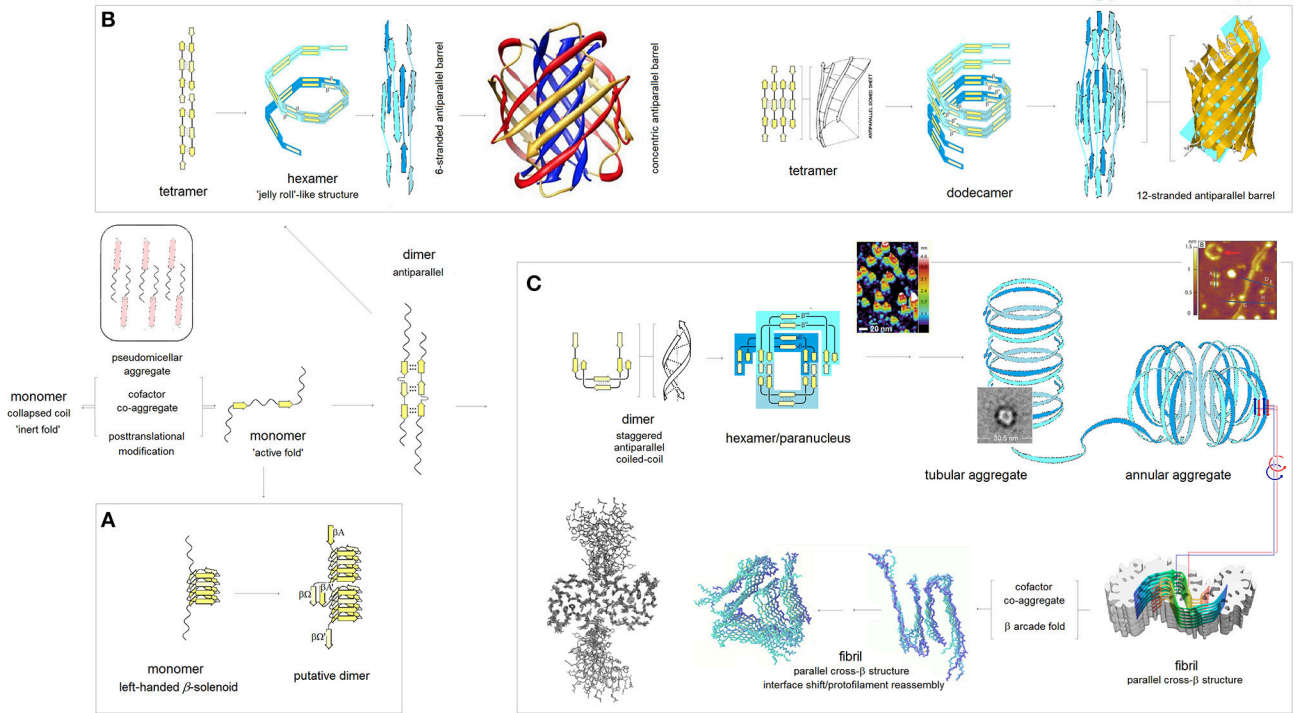

FIGURE 3 | The PMO theory of misfolding and aggregation of pleiomorphic proteins associated with common brain proteinopathies. Based on the PMO theory of protein secondary and tertiary structure (Cieplak, 2017) and conformational properties of β sheets (Salemme, 1983; Branden and Tooze, 1999), polymerization of Aβ, tau, αS and PrP^{C} is initiated by an "active" fold of the intrinsically disordered amyloidogenic region of a monomer. The "gain-of-structure" for the disordered region is realized either by folding into a β solenoid **(A)**, or coupled binding and folding into an antiparallel dimer by analogy to the coupled binding and folding of split inteins, which may lead to (i) antiparallel β barrel structures **(B)**, or (ii) parallel cross-β structures **(C)**. **(A)** Formation of the β solenoid structures: Folding of β solenoids is assumed to require the presence of a sequence of alternating "C_{7eq} strand" and "C_5 strand" propensities (in the parallel alignment, the free energy of the backbone-backbone H-bonding is minimized, according to the underlying PMO theory, by the binding backbone segments with *contrasting* "strand" propensities e.g., $C_{7eq}\uparrow C_5\uparrow$, cf. **Figure 2**), and a sequence of properly distributed residues capable of forming the stabilizing side-chain ladders (internal or external side-chain stacks, Branden and Tooze, 1999). So far, only the infectious PrP^{Sc} is reported to adopt such a structure (Vázquez-Fernández et al., 2016; Wille and Requena, 2018). **(B)** Formation of the antiparallel β-barrel structures: The register of the initial antiparallel homodimers is determined by the pattern of "strand" propensities since the free energy of backbone-backbone H-bonding, according to the underlying PMO theory, is minimized in the antiparallel alignment by binding backbone segments of *similar* "strand" propensities e.g., $C_5\uparrow C_5\downarrow$ or $C_{7eq}\uparrow C_{7eq}\downarrow$, cf. **Figure 2**. The head-to-tail aggregation of extended conformers of such antiparallel dimers and tetramers is assumed to yield oligomers which by a combination of twist, bend and rise can fold into "jelly-roll"-like cylindrical structures and subsequently into β barrels. Depending on the extension of its core, the initial barrel may convert into a concentric β barrel (Shafrir et al., 2010; Durell et al., 2018); while no such structures were actually isolated, this pathway seems to be consistent with a wide range of indirect evidence (Durell et al., 2018). **(C)** Formation of the parallel cross-β structures: The head-to-tail aggregation of coiled-coil conformers of the antiparallel dimers is assumed to yield circular wedge-shaped paranuclei (Fu et al., 2015; Economou et al., 2016); higher-order annular aggregates of such paranuclei are then expected to undergo conformational antiparallel-to-parallel β structure conversion to yield fibrils which assemble two protofilaments comprising parallel cross-β sheets and aligned in the antiparallel fashion (Schmidt et al., 2015). A collapse of a cross-β sheet onto itself, to form a β arcade, may lead to a separation of the two protofilaments and remodeling of the nascent fibrils into a wide range of alternative assemblies (Tycko, 2015; Colvin et al., 2016; Wälti et al., 2016). The inserted structure diagrams and AFM images are taken from the articles cited in the caption.

(e.g., C_{7eq} in **Figure 5Ca**) are not incorporated in the cross-β structure. Collapse of a cross-β sheet onto itself, to form a β arcade, may lead to a separation of the two protofilaments and remodeling of the nascent fibrils into a wide range of alternative assemblies. Regardless, *the core of the tau fibril is produced by conformational conversion of the antiparallel β structure of the initial homodimer: the composition of the core reflects the register and extension of the β structure of the homodimer.*

The mechanism of conformational conversion presented in **Figure 5** implies that the fibrillization of tau depends *inter alia* on the balance between the "C_5 strand" and "helix" propensities of R3. For instance, a significant increase in the "C_5 strand" propensity may facilitate initial formation of granular aggregates but hinder the subsequent antiparallel-to-parallel β structure conversion. Thus, substitutions, deletions, post-translational modifications etc. in the V306-K321 segment may facilitate or impede fibrillization depending on the effect on this balance. Indeed, replacement of a single residue within PHF6 may (i) modify morphology of filaments, (ii) prevent conversion of granular aggregates into filaments, or (iii) stop aggregation altogether (Naruto et al., 2010; Sogawa et al., 2012, 2014). In agreement with the mechanism in **Figure 5**, these outcomes tend to be consistent with the changes in the FP_i vs. $\Delta FP_{i-1\rightarrow i+1}$ plots, see **Figure 6**.

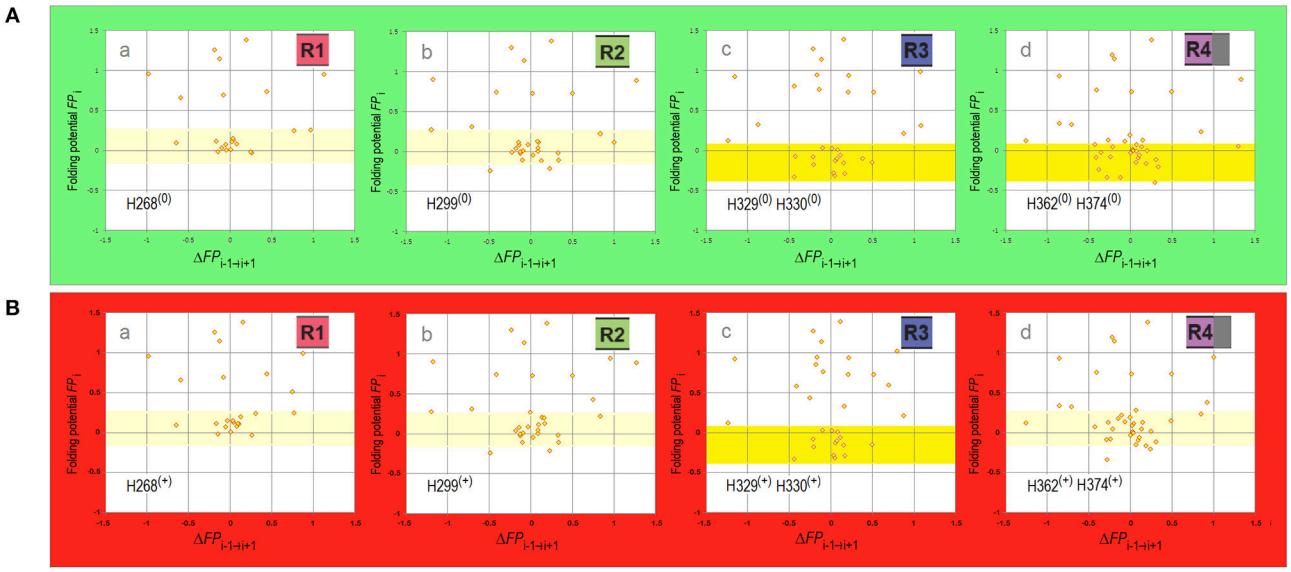

FIGURE 4 | Electronic configuration of the polypeptide backbone and secondary structure propensities of MTBD repeats. **(A)** The FP_i vs. $\Delta FP_{i-1\rightarrow i+1}$ plots for MTBD repeats calculated with $\sigma^{His} = -0.2917$. The region of FP_i color-coded pale yellow in R1 and R2 corresponds to the ambiguous "strand"/"helix" propensity in water, the region color-coded yellow in R3 and R4 corresponds to "C_5 strand" propensity in water. (a) Truncated R1, residues 252–274 (omitted the proline-rich segment ^{247}PVPMP^{251}); (b) R2, residues 275–305; (c) R3, residues 306–336; (d) Appended R4, residues 337–376 (appended ^{369}KKIETHKL^{376} segment incorporated in some fibril cores). **(B)** The FP_i vs. $\Delta FP_{i-1\rightarrow i+1}$ plots for MTBD repeats calculated with $\sigma^{His+} = 0.2584$. The data plotted for the same sequences identified above in **(A)**(a–d), and the FP_i regions color-coded as above, indicating water-bound ambiguous "strand"/"helix" propensity in R1, R2, and R4, and water-bound "C_5 strand" propensity in R3.

(ii) Electronic Configuration of the Polypeptide Backbone and the Divergent Pathways of Fibrillization of the 3R MTB Domain: Tau Inclusions in Alzheimer's, CTE and Pick's Disease

The cryo-EM investigation has recently shown that paired helical filaments of tau isolated from the brains of Pick's, Alzheimer's and chronic traumatic encephalopathy (CTE) patients are considerably different in their fibril-core structure (Fitzpatrick et al., 2017; Falcon et al., 2018, 2019). It is reported that only two repeats of 3R-tau (R1-R3R4) are retained in the core of PHFs isolated from the brains of the Alzheimer's and CTE patients, but all three repeats are incorporated in the fibril core of PHFs isolated from the brains of the Pick's patients; besides, the contact between the protofilaments occurs at different register, in the center of the third repeat in Pick's fold, and between the third and fourth repeats in the Alzheimer's fold and CTE fold type II. Here we demonstrate that these differences are consistent with the changes in the pattern of MTBD backbone polarization brought about by the protonation of His268 and His362.

First, we examine the FP_i plot for R1-R3R4 assuming that these two histidine side chains are not protonated ($\sigma^{His} = -0.2917$, **Table 1**), see **Figure 7A**a. The FP_i-based assignment of the anticipated secondary structure propensities is indeed in accord with the cryo-EM based assignment of β structure in the tau PHFs isolated from the Alzheimer's and CTE brains, see the "rainbow-color coded" bar immediately below the FP_i plot, the Alzheimer-fold diagram on the right-hand side, **Figure 7A**b, and the CTE-fold diagrams below, type II and I, **Figures 7A**d,e. Note that the CTE isolates are complexes of tau with a hydrophobic cofactor or cofactors; possibly that is why only the minor fraction, type II, retains the 2-fold symmetry of the hypothetical nascent fibril, while the major fraction, type I, lacks this symmetry because of an interface shift.

The expected antiparallel homodimer 3R↑3R↓ is shown in **Figure 7A**c. The register of dimerization is controlled by "matching" the anticipated "C_5 strands" i.e., the R3 and R4 repeats which have similar FP_i profiles under these conditions (cf. **Figure 4**): β1↑β8↓, β2↑β7↓ and β3↑β4↓. The segments L253-G276 (β0 in R1) and L346-K353 (β5 and β6 in R4) are not incorporated in the β antiparallel structure of the dimer, the first remaining "free," as the unattached "C_{7eq} strand," and the other forming a loop. The "free" β0 strand is essential to further aggregation via "domain swapping," cf. **Figure 5C**b, and would not be retained in the fibril core. The 2-fold axis of the anticipated homodimer structure is centered between the repeats R3 and R4, and this register correctly places the C322 residues far apart from each other, cf. **Figure 7A**b.

The results of polymerization of the truncated tau construct dGAE corroborate the proposed model. The PHFs assembly of dGAE occurs in 10 mM phosphate buffer, pH 7.4, in the absence of the anionic cofactors (Al-Hilaly et al., 2017). The dGAE construct comprises only two repeats but also, in addition, the C-terminal E372-E394 segment. In this construct, the repeats R3 and R4, and their FP_i profile ($\sigma^{His} = -0.2917$), see **Figure 7B**a,

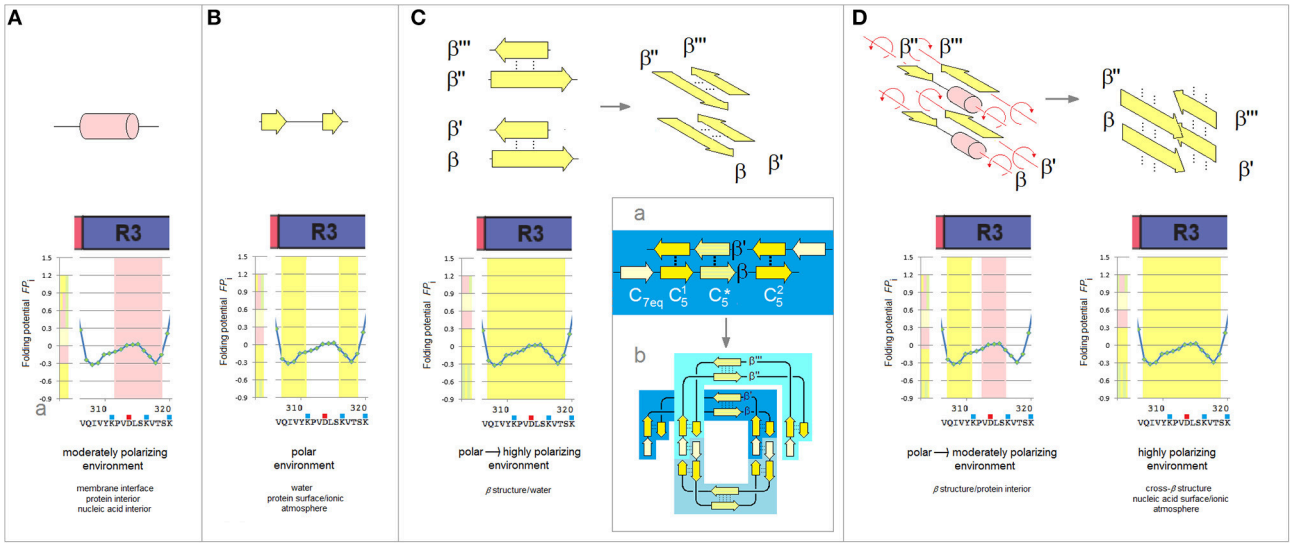

FIGURE 5 | The polarizing effect of the medium, secondary structure propensity of R3, and the mechanism of antiparallel-to-parallel β structure conversion as a path to paired helical filaments of tau. **(A)** The V306-K321segment of the third repeat is expected to fold into a "helix" in a moderately polarizing environment e.g., in the interior of a microtubule complex. The relation between the polarizing effect of the medium and the secondary structure propensity of the polypeptide backbone is indicated in these diagrams by the color-coded bars, cf. **Figure 1B**, juxtaposed with the FP_i plots. **(B)** The V306-K321 segment is expected to remain disordered in the aqueous buffers, see text. **(C)** The V306-K321 segment is stabilized in water in the "C_5 strand" configuration by the formation of a two-stranded antiparallel β sheet (binding and folding "gain-of-structure"). The two antiparallel β sheets can in principle be superposed in the parallel alignment as shown in the diagram on the right; (a) The archetypal 'productive' homodimer of the amyloidogenic region comprises three β-sheets $C_5^1\uparrow C_5^2\downarrow/C_5^*\uparrow C_5^*\downarrow/C_5^2\uparrow C_5^1\downarrow$ and is "appended" by the N-terminal "C_{7eq} strands"; (b) The head-to-tail aggregate of three homodimers folded into a disk-shaped paranucleus. Note the parallel alignment of the two superposed homodimers. **(D)** The V306-K321 segments lose the "C_5 strand" propensity and become disordered when they are placed in a poorly polarizing environment of the protein interior as a result of aggregation of the paranuclei. The antiparallel β sheets dissociate and the rotation about the strand axes yields parallel alignment of the V306-K321 segments. In the highly polarizing environment of the extended β-cross structure, cf. **Figure 1B**(d), these segments will again attain the "C_5 strand" configuration.

are identical to those in **Figure 7A**a. The repeat R1 is absent but its role as the "free" β0 strand can be assumed here by the C-terminal segment. Thus, the dGAE↑dGAE↓ homodimer is expected to have the same core of antiparallel β structure as the Alzheimer 3R↑3R↓ dimer, and similar capacity for further polymerization via "domain swapping." The C322s would be far apart in this homodimer, **Figure 7B**b, and indeed the assembly of dGAE PHFs is impeded under the non-reducing conditions at pH 7.4.

To consider now an alternative homodimer, we examine the FP_i plot for R1-R3R4 assuming that the side chains of His268 in R1 and His362 in R4 are protonated ($\sigma^{His+} = 0.2584$, **Table 1**), see **Figure 7C**a. As shown in **Figure 4**, the His362(^{0}) → His362($^+$) transition considerably alters the FP_i profile of R4 which is now similar to R1 rather than to R3. In fact, the new FP_i assignments of secondary structure propensity readily align with the β structure assignment for the tau PHFs isolated from the Pick's brains, see the "rainbow-color coded" bar below the FP_i plot, and the Pick-fold diagram on the right-hand side, **Figure 7C**b. Thus, at the moderately reduced pH, the register of dimerization is controlled by "matching" the anticipated "C_{7eq} strands" in R1 and R4 repeats: β1↑β8↓ and β2↑β7↓; this register is also stabilized by "matching" the "C_5 strands": β3↑β6↓ and β4↑β5↓, possibly β0↑β9↓ as well. As a result, all the repeats, including R1, are incorporated in the core of the antiparallel β structure of the homodimer, while the role of the "free" strand is assumed by the C-terminal segment, the β00 strand in the FP_i plot in **Figure 7C**a. The 2-fold axis of the dimer is now centered in the middle of the repeat R3 so that the C322 residues are in register, placed in the homodimer very close to each other, **Figure 7C**c.

Again, the results of polymerization of the truncated tau constructs, HPF47 and K19, corroborate the proposed model. Fibrillization of HPF47 and the K19 construct R1-R3R4 occurs in 50mM NH_4Ac buffer at pH 7.0, in the presence of the anionic cofactor heparin, and in both cases polymerization is accelerated under the non-reducing conditions (Friedhoff et al., 1998; von Bergen et al., 2000; Andronesi et al., 2008; Daebel et al., 2012). Assuming that the two histidine side chains are protonated under these conditions ($\sigma^{His+} = 0.2584$), the FP_i plot for PHF47 implies that the register of the homodimer does place the C322 residues very close to each other, see **Figures 7D**a,b. The FP_i plot for K19, **Figure 7E**a, shows that the core of the antiparallel β structure will incorporate all three repeats; the N-terminal segment of R1 assumes the role of the "free" β0 strand. The solid-state NMR data indicate that at least a part of R1 is indeed incorporated in the fibril core, **Figure 7E**b (Andronesi et al., 2008). In this case as well the C322 residues are placed very close to each other in the homodimer, **Figure 7E**c.

These data imply that one possible reason for the divergent fibrillization of tau in Alzheimer's and CTE disease on one hand, and Pick's disease on the other hand, may be the difference in

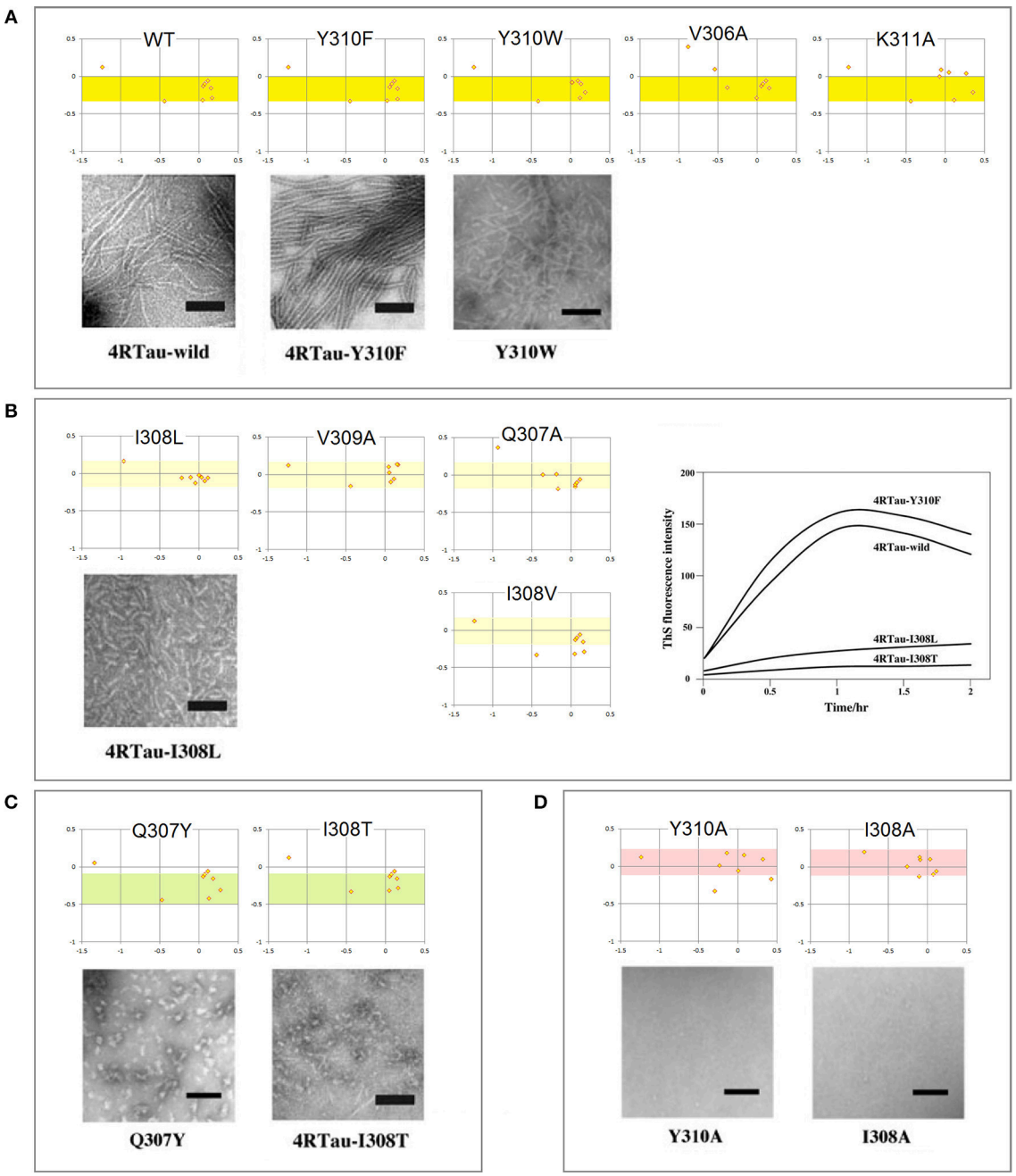

FIGURE 6 | Electronic configuration of the polypeptide backbone and aggregation properties of single-site mutants of tau PHF6: the FP_i vs. $\Delta FP_{i-1 \rightarrow i+1}$ plots and EM morphology. The results obtained by the heparin-induced fibrillization experiments conducted in Tris-HCl buffer at pH 7.6: **(A)** Mutants forming wild-type filaments. All the mutants retain the "C_5 strand" propensity of wt PHF6 (the yellow-color coded region of FP_i). **(B)** Mutants forming short filaments. The "C_5 strand" propensity of PHF6 tends to be attenuated compared to the wild type (the pale yellow-color coded region of FP_i); the plot on the right-hand side illustrates the effect of mutations on the intensity of thioflavin S fluorescence. **(C)** Mutants forming granules. The "C_5 strand" propensity of PHF6 tends to be increased compared to the wild type (the green-color coded region of FP_i). **(D)** Mutants forming neither granules nor filaments. The "C_5 strand" propensity of wt PHF6 is lost, replaced by the "helix" propensity (the red-color coded region of FP_i). The inserted images are taken from the articles cited in the text.

the environment's pH. Interestingly, tau pathology in Alzheimer's initially spreads from entorhinal cortex and locus coeruleus to the hippocampus (Goedert et al., 2017), and there are reports to suggests that the pH in the left hippocampus of Alzheimer's patients does increase rather than decrease in the age-related manner (Mecheri et al., 1997; Mandal et al., 2012; Cichocka et al., 2018). In contrast, the assembly of tau prions in Pick's disease would presumably be facilitated by a moderate drop in pH that

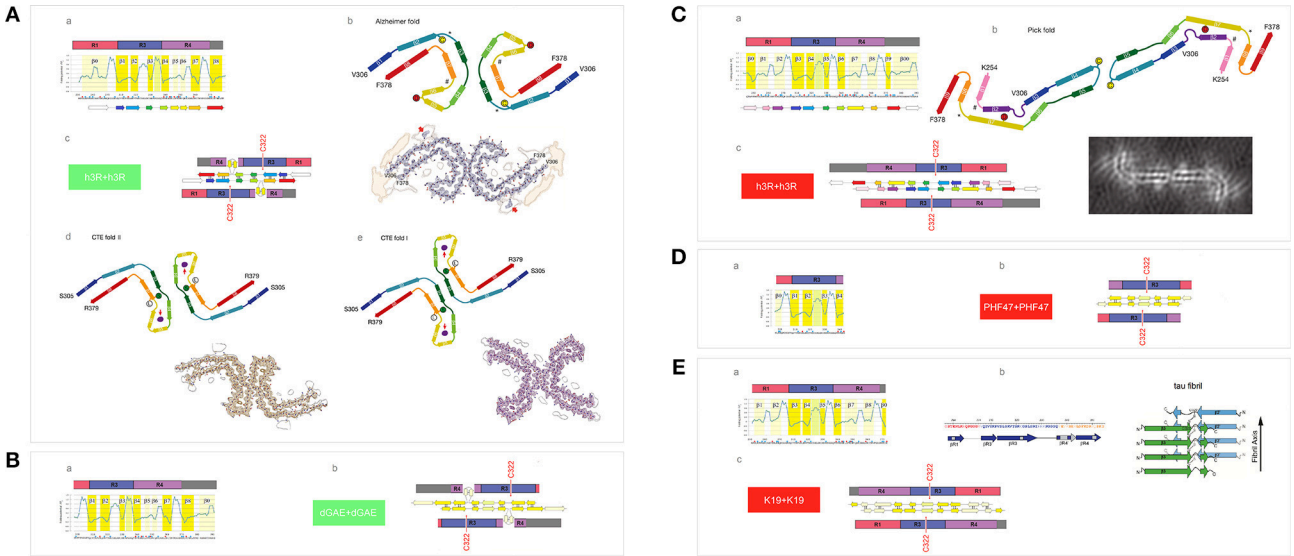

FIGURE 7 | Electronic configuration of the polypeptide backbone and divergent pathways of fibrillization of 3R isoforms: tau inclusions in Alzheimer's, CTE and Pick's disease. **(A)** (a) The FP_i profile of the tau repeat domain 3R (R1-R3R4), calculated with $\sigma^{His} = -0.2917$, indicates "C_5 strand" propensity of the segments: V306-K311(β1), L315-K321(β2), I328-H330(β3), V337-E342(β4), L357-H362(β7), K370-T377(β8). The FP_i assignment of the secondary-structure propensity is compared to the strand assignment in the Alzheimer's tau fold, see the "rainbow-color coded" bar immediately below the FP_i plot; (b) the Alzheimer-fold diagram, taken from Fitzpatrick et al. (2017); (c) a model of the seeding-competent antiparallel homodimer. Notice that the C322 residues are far apart in this dimer; (d) the CTE type-II, the fold diagram taken from Falcon et al. (2019), which apparently retains the 2-fold symmetry of the nascent fibril. Notice the presence of a hydrophobic co-factor encased (viz. the red arrow) in the protofilament's β arcade; (e) the CTE type-I, the fold diagram taken from Falcon et al. (2019). The structure apparently generated by the interface shift within the CTE type II PHFs. **(B)** (a) The FP_i profile of the truncated repeat-domain construct dGAE at pH 7.4. In the dGAE construct, the loss of the first repeat is compensated by the addition of a long C-terminal segment immediately following R4; (b) the corresponding model of the homodimer. **(C)** (a) The FP_i profile of the tau repeat domain 3R (R1-R3R4), calculated with $\sigma^{His+} = 0.2584$ for His268 and His362, shows the change from "C_5 strand" to "C_{7eq} strand" propensity in the segment L357-H362 [β8 vs. β7 in **(A)**(a)] and the enhancement of "C_{7eq} strand" propensity in the segment E263-Q269 [β2 vs. β0 in **(A)**(a)]. The FP_i assignment of the secondary-structure propensity is compared to the strand assignment in the Pick's tau fold, see the 'rainbow-color coded' bar immediately below the FP_i plot; (b) the Pick-fold diagram, taken from Falcon et al. (2018); (c) a model of the seeding-competent antiparallel homodimer. Notice that the shift from the "C_5 strand" to the "$C7_{eq}$ strand" propensity results in the change in register so that the C322 residues are now placed in the dimer in the immediate vicinity of each other. **(D)** (a) The FP_i profile of the truncated repeat-domain construct HPF47 calculated with $\sigma^{His+} = 0.2584$ for His268; (b) the homodimer. **(E)** (a) The FP_i profile of the truncated repeat-domain construct K19 calculated with $\sigma^{His+} = 0.2584$ for His268 and His362. The K19 construct has no C-terminal extension but retains the first repeat; (b) the solid-state NMR assignment of β structure in the fibril core; (c) the corresponding model of the homodimer.

accompanies e.g., transit in the endosomal system, inflammation response or an ischemic injury.

(iii) Electronic Configuration of the Polypeptide Backbone and Divergent Pathways of Fibrillization of 4R Isoforms: Heterogeneity of the Heparin-Induced Tau Fibrils and Asymmetric Cross-Seeding Barriers

The presence of an additional repeat segment in the 4R-tau isoforms increases the complexity of the aggregation pathways and raises the issue of co-aggregation and cross-seeding barriers. The recent cryo-EM investigation reveals that the heparin-induced fibrillization of 4R-tau in 30 mM MOPS at pH 7.2 (1 mM AEBSF, with 4 mM TCEP) yields a heterogeneous mixture of filaments formed by the second and third repeats only (Zhang et al., 2018). The plausible homodimer structures which account for the two most abundant PHFs are shown in **Figures 8A,C**. The first FP_i plot (**Figure 8A**a, $\sigma^{His} = -0.2917$) correctly anticipates the six β strands found in the 4R-snake fibrils, **Figure 8A**b. The fourth repeat is assumed to remain outside of the β structure of the homodimer, possibly folded into a β-sheet meander, **Figure 8A**c, or into a helix comprising the K340-K353 segment of R4; such a helix would be stabilized by the V337M mutation associated with the familial FTLD, see **Figure 8A**d. In any event, the 2-fold axis of the homodimer would be centered between the repeats R2 and R3 and only those two repeats would be incorporated in the fibril core, **Figures 8A**c,e.

So far, there is no report of the 4R fibrils that incorporate the R3-R4 rather than the R2-R3 repeats. The FP_i profile of the R2 repeat suggests however that the register of the 4R-tau homodimers can be redirected when a non-polar environment stabilizes helical conformations of the N279-Q288 segment, in particular when H299 is protonated, see **Figures 8B**a–c. Thus, some selective interactions with the protein, lipid, polyanionic cofactors or the membrane interface, or even selective polarizing or depolarizing interactions with other segments of tau molecule, could trigger such an alternative fibrillization pathway.

Presently, the reason for the difference in the register of 3R-tau dimers and heparin-induced 4R-tau dimers cannot be ascertained. One may note however that the free energy of

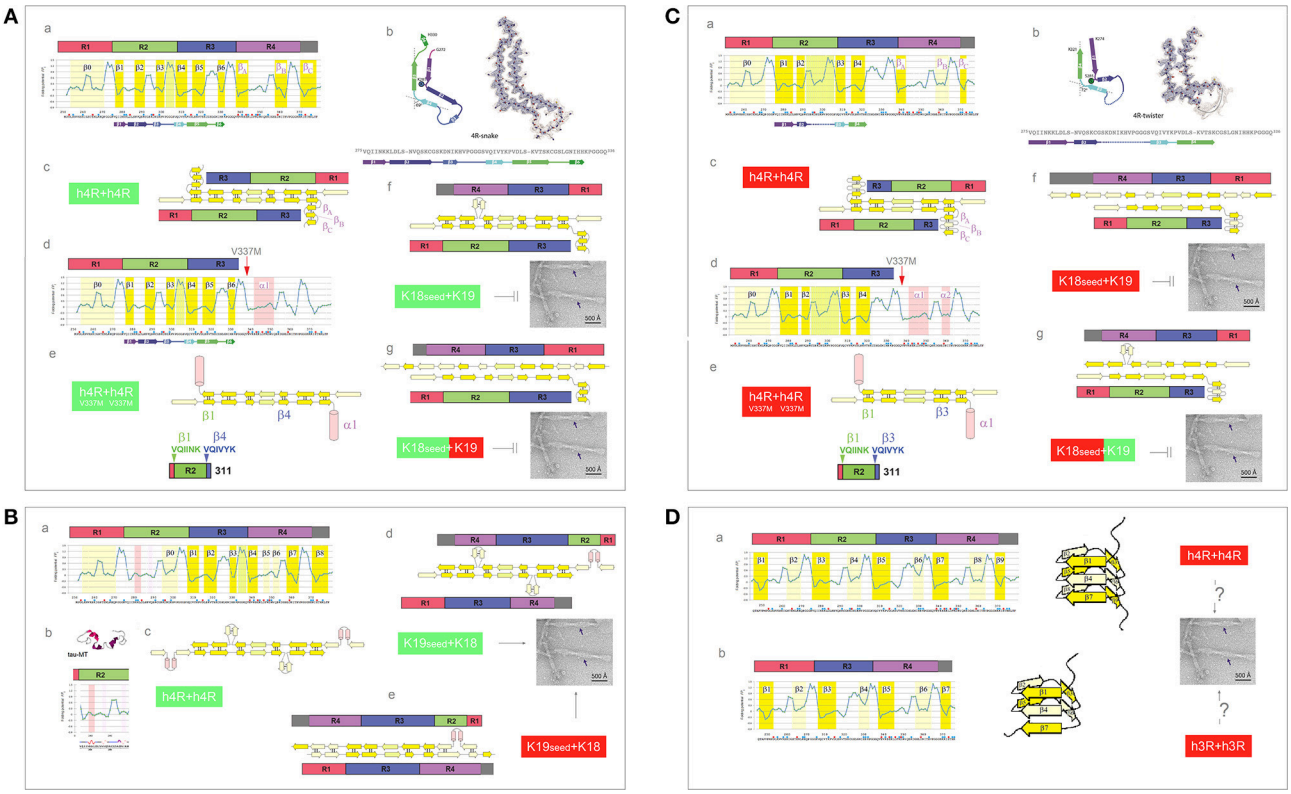

FIGURE 8 | Electronic configuration of the polypeptide backbone and divergent pathways of fibrillization of 4R isoforms: heterogeneity of the heparin-induced tau fibrils and asymmetric cross-seeding barriers. **(A)** (a) The FP_i profile of the tau repeat domain 4R (R1R2R3R4) calculated with $\sigma^{His} = -0.2917$. The FP_i assignment of the secondary-structure propensity is compared to the strand assignment in the 4R-snake fold of tau fibrils, see the color-coded bar immediately below the FP_i plot; (b) The diagram of the 4R-snake fold, taken from Zhang et al. (2018); (c) The corresponding model of the staggered antiparallel homodimer 4R↑4R↓; (d) The FP_i profile of the repeat domain 4R (R1R2R3R4) of the tau V337M. Note the change of the propensity of R4 into "helix"; (e) The corresponding model of the antiparallel homodimer 4R↑4R↓ with R4 folded into "helix"; (f) The model of the antiparallel "non-protonated" heterodimer 4R↑3R↓, notice the lack of 2-fold symmetry. The model implies that the K18 seeds cannot template oligomerization of K19 under these conditions; (g) The model of the antiparallel $3R(^{+})\downarrow 4R\uparrow$ heterodimer, notice the lack of 2-fold symmetry. The model implies that K18 seeds cannot template oligomerization of K19 under these conditions either. **(B)** (a) The FP_i profile of the tau repeat domain 4R (R1R2R3R4) calculated with $\sigma^{His+} = 0.2584$ for H299, and selectively induced into "helix" in R2; (b) The FP_i profile of R2 bound to microtubule as a "helix" bundle, PDB ID 2mz7; (c) The corresponding model of the staggered antiparallel homodimer 4R↑4R↓; (d) The model of the alternative "non-protonated" 3R↑4R↓ heterodimer. Notice that this heterodimer is seeding-competent according to the underlying PMO theory, **Figure 5**, which implies that the K19 seeds can template oligomerization of K18; (e) The model of the alternative "protonated" 3R↑4R↓ heterodimer. Notice that this heterodimer is seeding-competent according to the underlying PMO theory, **Figure 5**, which implies that the K19 seeds can template oligomerization of K18. **(C)** (a) The FP_i profile of the tau repeat domain 4R (R1R2R3R4) calculated with $\sigma^{His+} = 0.2584$. The FP_i assignment of the secondary-structure propensity is compared to the strand assignment in the 4R-twister fold of tau fibrils, see the color-coded bar immediately below the FP_i plot; (b) The diagram of the 4R-twister fold taken from Zhang et al. (2018); (c) The corresponding model of the staggered antiparallel homodimer 4R↑4R↓; (d) The FP_i profile of the repeat domain 4R (R1R2R3R4) of the tau mutant V337M. Notice the change of the propensity of 4R into "helix"; (e) The corresponding model of the antiparallel homodimer 4R↑4R↓ with R4 folded into "helix"; (f) The model of the protonated 3R↑4R↓ heterodimer. Notice that this heterodimer is *not* seeding-competent according to the underlying PMO theory, **Figure 5**, which implies that the "protonated" K18 seeds cannot template oligomerization of K19 under these conditions; (g) The model of the $4R(^{+})\uparrow 3R\downarrow$ heterodimer. Notice that this heterodimer is *not* seeding-competent according to the underlying PMO theory, **Figure 5**, which implies that the "protonated" K18 seeds cannot template oligomerization of K19 under these conditions either. **(D)** The FP_i plots illustrate the hypothetical patterns of "strand" propensities produced by protonation of MTBD histidines ($\sigma^{His+} = 0.2584$) which would be consistent with folding of MTBD into a β helix (cf. **Figure 3A**). In contrast to the antiparallel alignment, the parallel alignment of a two-stranded β sheet is stabilized, according to the underlying PMO theory see **Figure 2**, by the backbone-backbone H-bonding between two segments of *different* "strand" propensities e.g., $C_{7eq}\uparrow C_5\uparrow$. (a) 4R-tau isoform, the diagram shows the corresponding right-handed three-rung β solenoid; (b) 3R-tau isoform, the diagram shows the corresponding right-handed two-rung β solenoid.

backbone-backbone H-bonding could be minimized in the (R2-R3)↑(R2-R3)↓ complex rather than in the (R3-R4)↑(R3-R4)↓ complex, in spite of the more ambiguous "C_5 strand" in-water-propensity of R2 compared to R4, because of the more advantageous spacing of its "strand" segments. If this is indeed the case, it follows that the asymmetric barrier to cross-seeding of the truncated constructs K18 and K19 could result from the differences in backbone polarization of the MTBD repeats. Assuming that the "non-protonated" truncated 4R-tau construct K18 adopts the same configuration as the one shown in **Figure 8A**, K18 seeds are not expected to induce fibrillization of the truncated 3R-tau construct K19: the

hypothetical heterodimers lack the 2-fold symmetry and would not be stable enough to be "productive," see **Figures 8A**f,g. On the other hand, if the "non-protonated" K19 construct adopts the configuration as the one shown in **Figure 7A**, K19 seeds can template oligomerization of K18, see **Figure 8B**d; this might even be true for the "protonated" K19, **Figure 8B**e. Regardless, it seems that the 3R and 4R isoforms could co-aggregate under the conditions where His268 and His362 side chains remain neutral.

One plausible way to account for the second most abundant PHF in the heparin-induced fibril mixture, 4R-twister, is to consider protonation of MTBD histidines. The FP_i plot (**Figure 8C**a, $\sigma^{His+} = 0.2584$) does indeed correctly anticipate the four strands found in the "4R-twister" fibrils, **Figure 8C**b. The register of the homodimer is now shifted, the 2-fold axis is now centered in the middle of the repeat R2, while the repeat R4 is likely to fold into a coil or a helix, outside of the antiparallel β structure of the dimer, **Figures 8C**c–e. Note that the "helix" fold of the K340-K353 segment can also be stabilized by further drop in pH and $Glu^- \rightarrow Glu^0$ protonation (Cieplak, 2017). As for the experimental evidence of fibrillization at low pH, 4R-tau, and K18 were reported to form fibrils at pH 6.0 in the presence of polyglutamates (Nizynski et al., 2018), and aggregation of 4R-tau was reported to be slowed down in acetic acid buffer at pH 4.5 (Nishiura et al., 2010), while K19 is reported not to aggregate at pH 2.0 (Andronesi et al., 2008). As shown in the diagrams in **Figures 8C**d,e, the "protonated" 4R↑3R↓ heterodimers lack the 2-fold symmetry and would not be stable enough to be "productive"; accordingly, the 3R and 4R isoforms would not co-aggregate under these conditions.

Lastly, the FP_i plots for both isoforms protonated on all histidines (**Figure 8D**, $\sigma^{His+} = 0.2584$) suggest the emergence of the pattern of alternating "C_{7eq} strand" and "C_5 strand" propensities of MTBD. Hypothetically, this pattern is expected to facilitate formation of a β solenoid: in the parallel alignment of a two-stranded β sheet, the free energy of backbone-backbone H-bonding is minimized by binding the MTBD segments of *contrasting* "strand" propensities e.g., C_{7eq}↑C_5↑, cf. **Figures 2**, **3A**.

(iv) Electronic Configuration of the Polypeptide Backbone and the Aggregation Properties of the MAP Homologs

Tau belongs to the family of homologous microtubule-associated proteins, the closest homolog being MAP2c which, like tau, also forms granular aggregates. In contrast to tau, however, granular aggregates of MAP2c do not convert into fibrils. As was mentioned earlier in section (i), **Figure 5**, granular aggregates of tau may also lose the capacity to convert into fibrils as a result of a single-site mutation in the PHF6 segment. Interestingly, the FP_i plots point in both cases to the same underlying effect. The MTB domain of MAP2c comprises three repeats and so its FP_i profile can be directly compared to the FP_i profile of the 3R (R1-R3R4) isoform of tau, see **Figure 9A**. In view of the preceding discussion, one difference stands out amongst overall similarity of the two profiles, see the segment of MAP2c highlighted in red, **Figure 9A**b: in place of the ^{311}YKPV^{314} fragment of the third repeat of tau, the corresponding fragment in MAP2c has the sequence ^{340}TKKI^{343}. The replacement lowers the minimum of FP_i and removes the "strand"-perturbing Pro, and the two changes together significantly increase the "C_5 strand" propensity in water of the entire segment. As described in section (i), **Figure 5**, such an increase in the "C_5 strand" propensity may facilitate initial formation of granular aggregates but hinder the subsequent antiparallel-to-parallel β structure conversion. Accordingly, MAP2c forms granular aggregates but not fibrils (Xie et al., 2015), just like the PHF6 mutants of 3R-tau Q307Y and I308T which are also characterized by the increase in the "C_5 strand" propensity compared to the wild type, and form granular aggregates but not fibrils, cf. **Figure 6**.

It is sufficient, it turns out, to exchange the YKPV and TKKI tetrapeptides in the sequences of tau and MAP2c in order to completely reverse the aggregation properties of the two proteins: the 3R tau-TKKI mutant forms granular aggregates which do not convert into fibrils, while the MAP2c-YKPV mutant assembles into short fibrils, see **Figure 9B** (Xie et al., 2015). The change in "strand" propensity due to mutation is highlighted in the diagrams comparing the superposed FP_i profiles of the wild type and mutant proteins; this change is less obvious in the FP_i vs. $\Delta FP_{i-1\rightarrow i+1}$ plots, **Figure 9B**c. The FP_i plot for the MAP2c-YKPV mutant suggests however that the initial "productive" homodimer, **Figure 9B**d, would have somewhat different register than the 3R tau homodimer.

CONCLUDING REMARKS

The model of head-to-tail association of the antiparallel homodimers into disk-shaped hexamers, and subsequent antiparallel-to-parallel conversion of β structure within the aggregates of such hexamers, cf. **Figure 3**, was previously introduced (Cieplak, 2017) to account for the rates and morphology of Aβ aggregation on diverse surfaces (Kowalewski and Holtzman, 1999; Qing et al., 2014; Gao et al., 2015), obligatory micelle-like and helical intermediates of Aβ fibrillization (Yong et al., 2002; Roychaudhuri et al., 2009; Vitalis and Caflisch, 2010; Wälti et al., 2015), SAXS data on Aβ dimers (Ryan et al., 2015), AFM data on the morphology of early oligomerization states of Aβ (Fu et al., 2015; Economou et al., 2016), cryo-EM data on the morphology of Aβ fibrils (Schmidt et al., 2015), and the catalysis of fibrillogenesis by the intercalating aromatic ions (Williams et al., 2005; Ladiwala et al., 2011; Bieschke et al., 2012). The presented here outline of divergent pathways of the fibrillization of tau is based on the assumption that this model applies to tau as well. The reported recently broad diversity of the tau-fibril morphology (Fitzpatrick et al., 2017; Falcon et al., 2018, 2019; Zhang et al., 2018) is thus attributed to the variation in the register of the initial homodimers, a consequence of the variation in backbone polarization of the amyloidogenic region of tau which is determined by examination of the folding potential FP_i profiles. The sources of these variations are the very features which enable tau to perform its function: (i) the repeat structure of

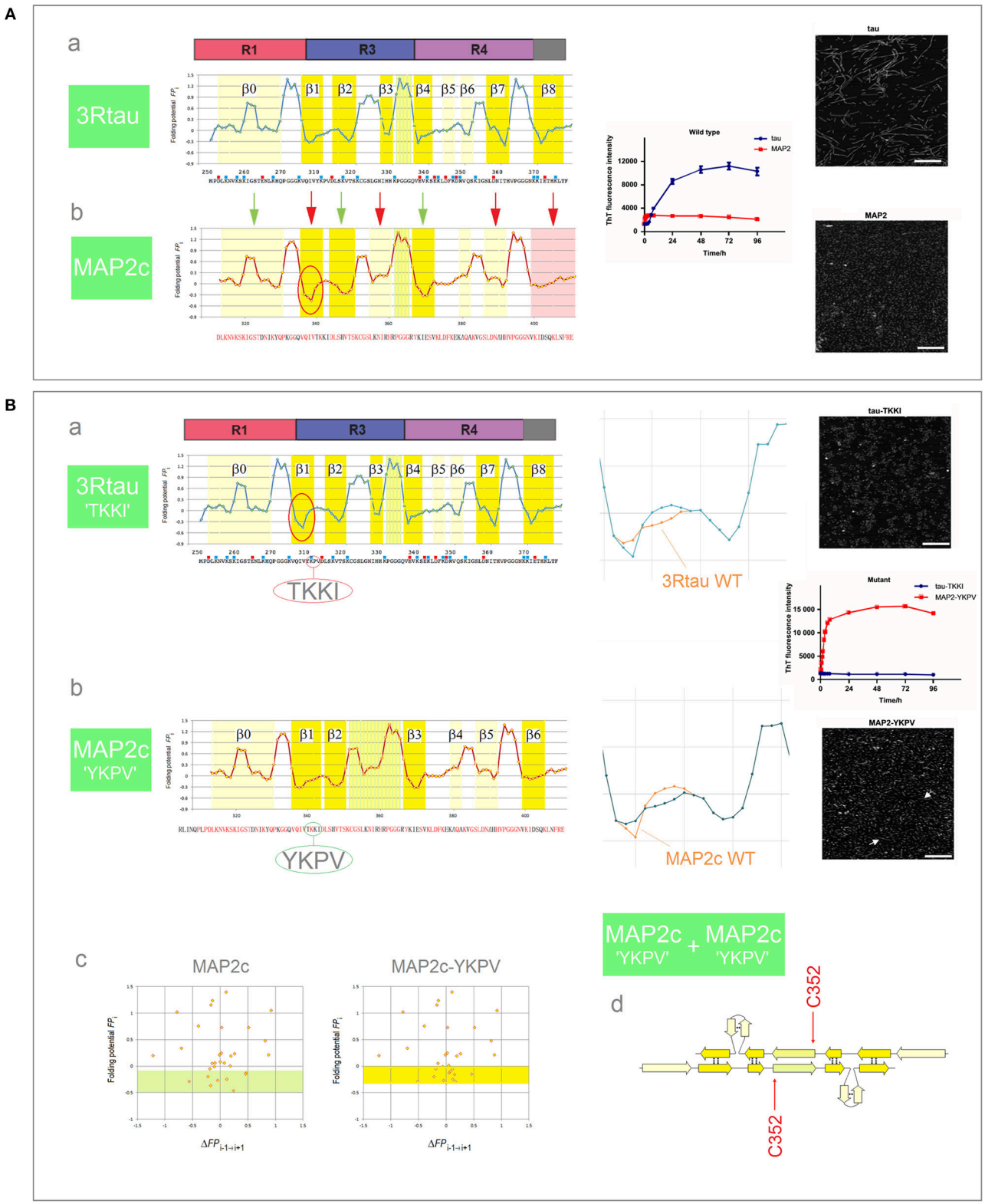

FIGURE 9 | Electronic configuration of the polypeptide backbone and the aggregation properties of MAP homologs. **(A)** (a) The FP_i profile of the 3R (R1-R3R4) isoform of tau and the anticipated secondary structure propensity in water. The adjacent plot of the ThT fluorescence intensity vs. time (blue curve) and the insert show the assembly of PHFs; (b) The FP_i profile of MAP2c and the anticipated secondary structure propensity in water. The adjacent plot (red curve) and the insert show that

(Continued)

FIGURE 9 | MAP2c does not form PHFs, polymerization stops at the stage of granular aggregates. The green and red arrows point to the retained and altered, respectively, secondary structure assignments; note the marked increase in the "C_5 strand" propensity in the segment corresponding to the V306-K321 segment of R3, see the text. **(B)** (a) The FP_i plot for 3R tau-TKKI mutant, see the text, and the anticipated secondary structure propensity in water. The right-hand diagram compares the superposed FP_i profiles of PHF6 in WT and mutant protein. The adjacent plot of the ThT fluorescence intensity vs. time (blue curve) and the insert show that the mutant does not form PHFs; (b) The FP_i plot for MAP2c-YKPV mutant, see the text, and the anticipated secondary structure propensity in water. The right-hand diagram compares the superposed FP_i profiles of the PHF6-like segment in WT and mutant protein. The adjacent plot of ThT fluorescence intensity vs. time (red curve) and the insert show the assembly of fibrils, viz. the white arrows in the insert; (c) The FP_i vs. $\Delta FP_{i-1\rightarrow i+1}$ plots for MAP2c and the MAP2c-YKPV mutant, note the shift in the "C_5 strand" propensity, up from the FP_i region characteristic for PHF6 mutants that form granular aggregates, **Figure 6C**, to the region characteristic for PHF6 mutants that form wild-type filaments, **Figure 6A**; (d) The anticipated "productive" homodimer of the MAP2c-YKPV mutant.

the amyloidogenic MTB domain marked by subtle differences in the electronic configuration of the repeats' main chain; (ii) ambiguous conformational propensities of the water-bound amyloidogenic region which make the fold of each separate segment of this region sensitive to the changes in polarity of the medium and molecular embedding i.e., to the selective binding of proteins, lipids, polyanionic cofactors, and selective polarizing or depolarizing interactions with other segments of the tau molecule; and (iii) the conserved His residues with the pK_a values in the physiological range (Charafeddine et al., 2019) which make conformational propensity of MTBD sensitive to a moderate drop in pH that accompanies for instance transit in the endosomal system, inflammation response or an ischemic injury.

Surprisingly, this account appears to capture major aspects of morphological diversity in tau fibrillization. It is surprising because the folding potential function FP_i focuses solely on the conformational and H-bonding propensity of the polypeptide backbone, ignoring side chain-side chain interactions. In fact, it would clearly be useful on some occasions to complement the FP_i plots by showing the distribution of the ionized side chains and potential "steric zipper" segments or the presence of proline and cysteine residues in the sequence. Thus, we do not comment in this paper on the posttranslational modifications and single-site mutations which alter MTBD charge or constrain main-chain geometry. Nonetheless, the outcome of the present investigation does suggest that the interactions dependent on backbone density distribution play an important role in conformational behavior of MTBD. This conclusion is in line with the arguments of the backbone-based theory of protein folding (Rose et al., 2006), and with the notion of common origin of amyloidogenicity of proteins associated with major brain proteinopathies.

AUTHOR CONTRIBUTIONS

The author confirms being the sole contributor of this work and has approved it for publication.

ACKNOWLEDGMENTS

We thank the administrators of the High-Performance Computer Center at Bilkent University for the assistance in realization of this project. The parallelized version of Gaussian 98, Revision A.7, was installed on the Sun Enterprise 4500 Server by Professor Ulrike Salzner of the Department of Chemistry, Bilkent University. We also thank Professor Kenneth B. Wiberg of the Department of Chemistry, Yale University, for the support and access to the departmental computing facilities.

REFERENCES

Adams, S. J., DeTure, M. A., McBride, M., Dickson, D. W., and Petrucelli, L. (2010). Three-repeat isoforms inhibit assembly of four repeat tau filaments. *PLoS ONE* 5:e10810. doi: 10.1371/journal.pone.0010810

Al-Hilaly, Y. K., Pollack, S. J., Vadukul, D. M., Citossi, F., Rickard, J. E., Simpson, M., et al. (2017). Alzheimer's disease-like paired helical filament assembly is independent of disulfide crosslinking. *J. Mol. Biol.* 429, 3650–3665. doi: 10.1016/j.jmb.2017.09.007

Andronesi, O. C., von Bergen, M., Biernat, J., Seidel, K., Griesinger, C., Mandelkow, E., et al. (2008). Characterization of Alzheimer's-like paired helical filaments from the core domain of tau protein using solid-state NMR spectroscopy. *J. Am. Chem. Soc.* 130, 5922–5928. doi: 10.1021/ja7100517

Ayers, J. I., Giasson, B. I., and Borschelt, D. R. (2018). Prion-like spreading in tauopathies. *Biol. Psychiatry* 83, 337–346. doi: 10.1016/j.biopsych.2017.04.003

Baldwin, R. L., and Rose, G. D. (1999). Is protein folding hierarchic? I. Local structure and peptide folding. *Trends Biochem. Sci.* 24, 26–33. doi: 10.1016/S0968-0004(98)01346-2

Bemporad, F., and Chiti, F. (2012). Protein misfolded oligomers: experimental approaches, mechanism of forming, and structure-toxicity relationships. *Chem. Biol.* 19, 315–327. doi: 10.1016/j.chembiol.2012.02.003

Bieschke, J., Herbst, M., Wiglenda, T., Friedrich, R. P., Boeddrich, A., Schiele, F., et al. (2012). Small-molecule conversion of toxic oligomers to non-toxic β-sheet-rich amyloid fibrils. *Nat. Chem. Biol.* 8, 93–101. doi: 10.1038/nchembio.719

Bradshaw, N. J., and Korth, C. (2018). Protein misassembly and aggregation as potential convergence points for non-genetic causes of chronic mental illness. *Mol. Psychiatry*. doi: 10.1038/s41380-018-0133-2

Branden, C., and Tooze, J. (1999). *Introduction to Protein Structure*. New York, NY: Garland Publishing, Inc.

Charafeddine, R. A., Cortopassi, W. A., Lak, P., Jacobson, M. P., Barber, D. L., and Witmann, T. (2019). Tau repeat regions contain conserved histidine residues that modulate microtubule-binding in response to changes in pH. *bioRxiv*. doi: 10.1074/jbc.RA118.007004 [Epub ahead of print].

Cichocka, M., Kozub, J., and Urbanik, A. (2018). Brain aging: evaluation of pH using phosphorus magnetic resonance spectroscopy. *Geriatr. Gerontol. Int.* 18, 881–885. doi: 10.1111/ggi.13272

Cieplak, A. S. (2017). Protein folding, misfolding and aggregation: the importance of two-electron stabilizing interactions. *PLoS ONE* 12:e0180905. doi: 10.1371/journal.pone.0180905

Cieplak, A. S., and Sürmeli, N. B. (2004). Single-site mutation and secondary structure stability: an isodesmic reaction approach. The case of unnatural amino acid mutagenesis Ala→ Lac. *J. Org. Chem.* 69, 3250–3261. doi: 10.1021/jo0358372

Colvin, M. T., Silvers, R., Ni, Q. Z., Can, T. V., Sergeyev, I., Rosay, M., et al. (2016). Atomic resolution structure of monomorphic Aβ42 amyloid fibrils. *J. Am. Chem. Soc.* 138, 9663–9674. doi: 10.1021/jacs.6b05129

Daebel, V., Chinnathambi, S., Biernat, J., Schwalbe, M., Habenstein, B., Loquet, A., et al. (2012). *J. Am. Chem. Soc.* 134, 13982–13989. doi: 10.1021/ja305470p

de Alba, E., Santoro, J., Rico, M., and Jimenez, M. A. (1999). *De novo* design of a monomeric three-stranded antiparallel β-sheet. *Protein Sci.* 8, 854–865. doi: 10.1110/ps.8.4.854

Debye, P., and Hückel, E. (1923). Zur Theorie der Elektrolyte. I. Gefrierpunktsernidrigung und verwandte Erscheinungen. *Phys. Zeit.* 24, 185–206.

del Carmen Cárdenas-Aguayo, M., Gómez-Virgilio, L., DeRosa, S., and Meraz-Rios, M. A. (2014). The role of tau oligomers in the onset of Alzheimer's disease neuropathology. *ACS Chem. Neurosci.* 5, 1178–1191. doi: 10.1021/cn500148z

Demaegd, K., Schymkowitz, J., and Rousseau, F. (2018). Transcellular spreading of tau in tauopathies. *Chembiochem* 19, 2424–2432. doi: 10.1002/cbic.201800288

Dujardin, S., Bégard, S., Caillierez, R., Lachaud, C. V., Carrier, S., Lieger, S., et al. (2018). Different tau species lead to heterogeneous tau pathology propagation and misfolding. *Acta Neuropathol. Commun.* 6:132. doi: 10.1186/s40478-018-0637-7

Durell, S. R., Kayed, R., and Guy, H. R. (2018). Theory of concentric β -barrel structures: models of amyloid beta 42 oligomers, annular protofibrils, and transmembrane channels. *bioRxiv*. doi: 10.1101/49906

Economou, N. J., Giammona, M. J., Do, T. D., Zheng, X., Teplow, D. B., Buratto, S. K., et al. (2016). Amyloid β-protein assembly and Alzheimer's disease: dodecamers of Aβ42, but not of Aβ40, seed fibril formation. *J. Am. Chem. Soc.* 138, 1772–1775. doi: 10.1021/jacs.5b11913

Edgcomb, S. P., and Murphy, K. P. (2002). Variability in pK_a of histidine side-chains correlates with burial within proteins. *Proteins* 49, 1–6. doi: 10.1002/prot.10177

Eryilmaz, E., Shah, N. H., Muir, T. W., and Cowburn, D. (2014). Structural and dynamic features of inteins and implication on protein splicing. *J. Biol. Chem.* 289, 14506–14511. doi: 10.1074/jbc.R113.540302

Eschmann, N. A., Georgieva, E. R., Ganguly, P., Borbat, P. P., Rappaport, M. D., Akdogan, Y., et al. (2017). Signature of an aggregation-prone conformation of tau. *Sci. Rep.* 7:44739. doi: 10.1038/srep44739

Falcon, B., Zhang, W., Murzin, A. G., Murshudov, G., Garringer, H. J., Vidal, R., et al. (2018). Structures of filaments from Pick's disease reveal a novel tau protein fold. *Nature* 561, 137–140. doi: 10.1038/s41586-018-0454-y

Falcon, B., Zivanov, J., Zhang, W., Murzin, A. G., Garringer, H. J., Vidal, R., et al. (2019). Novel tau filament fold in chronic traumatic encephalopathy encloses hydrophobic molecules. *Nature* 568, 420–423. doi: 10.1038/s41586-019-1026-5

Fichou, Y., Vigers, M., Goring, A. K., Eschmann, N. A., and Han, S. (2018). Heparin-induced tau filaments are structurally heterogeneous and differ from Alzheimer's disease filaments. *Chem. Commun.* 54, 4573–4576. doi: 10.1039/C8CC01355A

Fisk, J. D., Schmitt, M. A., and Gellman, S. H. (2006). Thermodynamic analysis of autonomous parallel β-sheet formation in water. *J. Am. Chem. Soc.* 128, 7148–7149. doi: 10.1021/ja060942p

Fitzpatrick, A. W. P., Falcon, B., He, S., Murzin, A. G., Murshudov, G., Garringer, H. J., et al. (2017). Cryo-EM structures of tau filaments from Alzheimer's disease brain. *Nature* 547, 185–190. doi: 10.1038/nature23002

Friedhoff, P., von Bergen, M., Mandelkow, E.-M., Davies, P., and Mandelkow, E. (1998). A nucleated assembly mechanism of Alzheimer paired helical filaments. *Proc. Natl. Acad. Sci. U.S.A.* 95, 15712–15717. doi: 10.1073/pnas.95.26.15712

Frisch, M. J., Trucks, G. W., Schlegel, H. B., Scuseria, G. E., Robb, M. A., Cheeseman, J. R., et al. (1998). *Gaussian 98 Revision A.3*. Pittsburgh, PA: Gaussian Inc.

Fu, Z., Aucoin, D., Davis, J., Van Nostrand, W. E., and Smith, S. O. (2015). Mechanism of nucleated conformational conversion of Aβ42. *Biochemistry* 54, 4197–4207. doi: 10.1021/acs.biochem.5b00467

Gao, G., Zhang, M., Lu, P., Guo, G., Wang, D., and Sun, T. (2015). Chirality assisted ring-like aggregation of Aβ(1-40) at liquid-solid interfaces: a stereoselective two-step assembly process. *Angew. Chem. Int. Ed.* 54, 2245–2250. doi: 10.1002/anie.201410768

Gao, Y.-L., Wang, N., Sum, F.-R., Cao, X.-P., Zhang, W., Yu, J.-T., et al. (2018). Tau in neurodegenerative disease. *Ann. Transl. Med.* 6:175. doi: 10.21037/atm.2018.04.23

Goedert, M., Masuda-Suzukake, M., and Falcon, B. (2017). Like prions: the propagation of aggregated tau and α-synuclein in neurodegeneration. *Brain* 140, 266–278. doi: 10.1093/brain/aww230

Goedert, M., and Spillantini, M. G. (2017). Propagation of tau aggregates. *Mol. Brain* 10:18. doi: 10.1186/s13041-017-0298-7

Griffiths-Jones, S. R., and Searle, M. S. (2000). Structure, folding, and energetics of cooperative interactions between the β-strands of a *de novo* designed three-stranded antiparallel β-sheet peptide. *J. Am. Chem. Soc.* 122, 8350–8356. doi: 10.1021/ja000787t

Guo, T., Noble, W., and Hanger, D. P. (2017). Roles of tau protein in health and disease. *Acta Neuropathol.* 133, 665–704. doi: 10.1007/s00401-017-1707-9

Hasegawa, M. (2016). Molecular mechanisms in the pathogenesis of Alzheimer's disease and tauopathies – prion-like seeded aggregation and phosphorylation. *Biomolecules* 6:24. doi: 10.3390/biom6020024

Huang, R. Y., Iacob, R. E., Sankaranarayanan, S., Yang, L., Ahlijanian, M., Tao, L., et al. (2018). Probing conformational dynamics of tau protein by hydrogen/deuterium exchange mass spectrometry. *J. Am. Soc. Mass Spectrom.* 29, 174–182. doi: 10.1007/s13361-017-1815-8

Karikari, T. K., Nagel, D. A., Grainger, A., Clarke-Bland, C., Hill, E. J., and Moffat, K. G. (2019). *Anal. Biochem.* 566, 67–74. doi: 10.1016/j.ab.2018.10.013

Kjaergaard, M., Dear, A. J., Kundel, F., Qamar, S., Meisl, G., Knowles, T. P. J., et al. (2018). Oligomer diversity during aggregation of the repeat region of tau. *ACS Chem. Neurosci.* 9, 3060–3071. doi: 10.1021/acschemneuro.8b00250

Kowalewski, T., and Holtzman, D. M. (1999). *In situ* atomic force microscopy study of Alzheimer's β-amyloid peptide on different substrates: new insights into mechanism of β-sheet formation. *Proc. Natl. Acad. Sci. U S A.* 96, 3688–3693. doi: 10.1073/pnas.96.7.3688

Kumar, H., and Udgaonkar, J. B. (2018). Mechanistic and structural origins of the asymmetric barrier to prion-like cross-seeding between tau-3R and tau-4R. *J. Mol. Biol.* 430, 5304–5312. doi: 10.1016/j.jmb.2018.09.010

Kumar, S., Tepper, K., Kaniyappan, S., Biernat, J., Wegmann, S., Mandelkow, E.-M., et al. (2014). Stages and conformations of the tau repeat domain during aggregation and its effects on neuronal toxicity. *J. Biol. Chem.* 289, 20318–20332. doi: 10.1074/jbc.M114.554725

Kung, V. M., Cornilescu, G., and Gellman, S. H. (2015). Impact of strand number on parallel β-sheet stability. *Angew. Chem. Int. Ed.* 54, 14336–14339. doi: 10.1002/anie.201506448

Kyte, J. (1995). *Structure in Protein Chemistry*. New York, NY; London: Garland Publishing, Inc.

Ladiwala, A. R., Dordick, J. S., and Tessier, P. M. (2011). Aromatic small molecules remodel toxic soluble oligomers of amyloid β through three independent pathways. *J. Biol. Chem.* 286, 3209–3219. doi: 10.1074/jbc.M110.173856

Lathuillière, A., Valdés, P., Papin, S., Cacquerel, M., Maclachlan, C., Knott, G. W., et al. (2017). Motifs in the tau protein that control binding to microtubules and aggregation determine pathological effects. *Sci. Rep.* 7:13556. doi: 10.1038/s41598-017-13786-2

Lopez de la Paz, M., Lacroix, E., Ramirez-Alvarado, M., and Serrano, L. (2001). Computer-aided design of β-sheet peptides. *J. Mol. Biol.* 312, 229–246. doi: 10.1006/jmbi.2001.4918

Macdonald, J. A., Bronner, I. F., Drynan, L., Fan, J., Curry, A., Fraser, G., et al. (2019). Assembly of transgenic human P301S Tau is necessary for neurodegeneration in murine spinal cord. *Acta Neuropathol. Commun.* 7:44. doi: 10.1186/s40478-019-0695-5

Maeda, S., Sahara, N., Saito, Y., Murayama, M., Yoshike, Y., Kim, H., et al. (2007). Granular tau oligomers as intermediates of tau filaments. *Biochemistry* 46, 3856–3861. doi: 10.1021/bi061359o

Mandal, P. K., Akolkar, H., and Tripathi, M. (2012). Mapping of hippocampal pH and neurochemicals from *in vivo* multi-voxel ^{31}P study in healthy normal young male/female, mild cognitive impairment, and Alzheimer's disease. *J. Alzheimer's Dis.* 31, S75–S86. doi: 10.3233/JAD-2012-120166

Mecheri, G., Marie-Cardine, M., Sappey-Marinier, D., Bonmartin, H., Albrand, G., Ferry, G., et al. (1997). *In vivo* hippocampal ^{31}P NMR metabolites in Alzheimer's disease and aging. *Eur. Psychiatry* 12, 140–148. doi: 10.1016/S0924-9338(97)80203-9

Minoura, K., Tomoo, K., Ishida, T., Hasegawa, M., Sasaki, M., and Taniguchi, T. (2003). Solvent-dependent conformation of the third repeat fragment in the microtubule-binding domain of tau protein, analyzed by ^{1}H NMR

spectroscopy and molecular modeling calculations. *Bull. Chem. Soc. Jpn.* 76, 1617–1624. doi: 10.1246/bcsj.76.1617

Mirbaha, H., Chen, D., Morazova, O. A., Ruff, K. M., Sharma, A. M., Liu, X., et al. (2018). Inert and seed-competent tau monomers suggest structural origins of aggregation. *Elife* 7:36584. doi: 10.7554/eLife.36584

Miyagi, M., and Nakazawa, T. (2008). Determination of pK_a values of individual histidine residues in proteins using mass spectrometry. *Anal. Chem.* 80, 6481–6487. doi: 10.1021/ac8009643

Naruto, K., Minoura, K., Okuda, T., In, Y., Ishida, T., and Tomoo, K. (2010). Interplay between I308 and Y310 residues in the third repeat of microtubule-binding domain is essential for tau filament formation. *FEBS Lett.* 584, 4233–4236. doi: 10.1016/j.febslet.2010.09.012

Nishiura, C., Takeuchi, K., Minoura, K., Sumida, M., Taniguchi, T., Tomoo, K., et al. (2010). Importance of Tyr310 residue in the third repeat of microtubule binding domain for filament formation of tau protein. *J. Biochem.* 147, 405–414. doi: 10.1093/jb/mvp181

Nizynski, B., Dzwolak, W., and Nieznanski, K. (2017). Amyloidogenesis of tau protein. *Protein Sci.* 26, 2126–2150. doi: 10.1002/pro.3275

Nizynski, B., Nieznanska, H., Dec, R., Boyko, S., Dzwolak, W., and Nieznanski, K. (2018). Amyloidogenic cross-seeding of tau protein: transient emergence of structural variants of fibrils. *PLoS ONE* 13:e0201182. doi: 10.1371/journal.pone.0201182

Onsager, L. (1936). Electric moments of molecules in liquids. *J. Am. Chem. Soc.* 58, 1486–1493. doi: 10.1021/ja01299a050

Pavlova, A., Cheng, C.-Y., Kinnebrew, M., Lew, J., Dahlquist, F. W., and Han, S. (2016). Protein structural and surface water rearrangement constitute major events in the earliest aggregation stage of tau. *Proc. Natl. Acad. Sci. U S A.* 113, E127–E136. doi: 10.1073/pnas.1504415113

Perez, M., Santa-Maria, I., Tortosa, E., Cuadros, R., del Valle, M., Hernández, F., et al. (2007). The role of the VQIVYK peptide in tau protein phosphorylation. *J. Neurochem.* 103, 1447–1460. doi: 10.1111/j.1471-4159.2007.04834.x

Perez, M., Valpuesta, J. M., Medina, M., Montejo de Garcini, E., and Avila, J. (1996). Polymerization of tau into filaments in the presence of heparin: the minimal sequence required for tau-tau interaction. *J. Neurochem.* 67, 1183–1190. doi: 10.1046/j.1471-4159.1996.67031183.x

Qing, G., Zhao, S., Xiong, Y., Jiang, F., Liu, Y., Chen, H., et al. (2014). Chiral effect at protein/graphene interface: a bioinspired perspective to understand amyloid formation. *J. Am. Chem. Soc.* 136, 10736–10742. doi: 10.1021/ja5049626

Ren, Y., and Sahara, N. (2013). Characteristics of tau oligomers. *Front. Neurol.* 4:102. doi: 10.3389/fneur.2013.00102

Rose, G. D., Fleming, P. J., Banavar, J. R., and Maritan, A. (2006). A backbone-based theory of protein folding. *Proc. Natl. Acad. Sci. U S A.* 103, 16623–16633. doi: 10.1073/pnas.0606843103

Roychaudhuri, R., Yang, M., Hoshi, M. M., and Teplow, D. B. (2009). Amyloid β-protein assembly and Alzheimer disease. *J. Biol. Chem.* 284, 4749–4753. doi: 10.1074/jbc.R800036200

Ryan, T. M., Roberts, B. R., McColl, G., Hare, D. J., Doble, P. A., Lin, Q. X., et al. (2015). Stabilization of nontoxic Aβ-oligomers: insights into the mechanism of action of hydroxyquinolines in Alzheimer's disease. *J. Neurosci.* 35, 2871–2884. doi: 10.1523/JNEUROSCI.2912-14.2015

Salemme, F. R. (1983). Structural properties of protein β-sheets. *Prog. Biophys. Mol. Biol.* 42, 95–133. doi: 10.1016/0079-6107(83)90005-6

Sanders, D. W., Kaufman, S. K., DeVos, S. L., Sharma, A. M., Mirbaha, H., Li, A., et al. (2014). Distinct tau prion strains propagate in cells and mice and define different tauopathies. *Neuron* 82, 1271–1288. doi: 10.1016/j.neuron.2014.04.047

Schmidt, M., Rohou, A., Lasker, K., Yadav, J. K., Schiene-Fischer, C., Fändrich, M., et al. (2015). Peptide dimer structure in an Aβ(1-42) fibril visualized with cryo-EM. *Proc. Natl. Acad. Sci. U S A.* 112, 11858–11863. doi: 10.1073/pnas.1503455112

Sebastián-Serrano, A., de Diego-García, L., and Díaz-Hernández, M. (2018). The neurotoxic role of extracellular tau protein. *Int. J. Mol. Sci.* 19:998. doi: 10.3390/ijms19040998

Shafrir, Y., Durell, S. R., Anishkin, A., and Guy, H. R. (2010). Beta-barrel models of soluble amyloid beta oligomers and annular protofibrils. *Proteins* 78, 3458–3472. doi: 10.1002/prot.22832

Shah, N. H., Eryilmaz, E., Cowburn, D., and Muir, T. W. (2013). Naturally split inteins assemble through a 'capture and collapse' mechanism. *J. Am. Chem. Soc.* 135, 18673–18681. doi: 10.1021/ja4104364

Sharma, A. M., Thomas, T. L., Woodard, D. R., Kashmer, O. M., and Diamond, M. I. (2018). Tau monomer encodes strains. *Elife* 7:e37813. doi: 10.7554/eLife.37813

Sheridan, R. P., Lee, R. H., Peters, N., and Allen, L. C. (1979). Hydrogen-bond cooperativity in protein secondary structure. *Biopolymers* 18, 2451–2458. doi: 10.1002/bip.1979.360181006

Siddiqua, A., Luo, Y., Meyer, V., Swanson, M. A., Yu, X., Wei, G., et al. (2012). Conformational basis for asymmetric seeding barriers in filaments of three- and four-repeat tau. *J. Am. Chem. Soc.* 134, 10271–10278. doi: 10.1021/ja303498q

Sogawa, K., Minoura, K., In, Y., Ishida, T., Taniguchi, T., and Tomoo, K. (2014). CH-π interaction in VQIVYK sequence elucidated by NMR spectroscopy is essential for PHF formation of tau. *Biopolymers* 102, 288–295. doi: 10.1002/bip.22489

Sogawa, K., Okuda, R., In, Y., Ishida, T., Taniguchi, T., Minoura, K., et al. (2012). C-H…π interplay between Ile308 and Tyr310 residues in the third repeat of microtubule binding domain is indispensable for self-assembly of three- and four-repeat tau. *J. Biochem.* 152, 221–229. doi: 10.1093/jb/mvs061

Sugino, E., Nishiura, C., Minoura, K., In, Y., Sumida, M., Taniguchi, T., et al. (2009). Three-/four-repeat dependent aggregation profile of tau microtubule-binding domain clarified by dynamic light-scattering analysis. *Biochem. Biophys. Res. Commun.* 385, 236–240. doi: 10.1016/j.bbrc.2009.05.047

Tokimasa, M., Minoura, K., Hiraoka, S., Tomoo, K., Sumida, M., Taniguchi, T., et al. (2005). Importance of local structures of second and third repeat fragments of microtubule binding domain for tau filament formation. *FEBS Lett.* 579, 3481–3486. doi: 10.1016/j.febslet.2005.05.020

Tycko, R. (2015). Amyloid polymorphism: structural basis and neurobiological relevance. *Neuron* 86, 632–645. doi: 10.1016/j.neuron.2015.03.017

Vázquez-Fernández, E., Vos, M. R., Afanasjev, P., Cebey, L., Sevillano, A. M., Vidal, E., et al. (2016). The structural architecture of an infectious mammalian prion using electron cryomicroscopy. *PLoS Pathog.* 12:e1005835. doi: 10.1371/journal.ppat.1005835

Vitalis, A., and Caflisch, A. (2010). Micelle-like architecture of the monomer ensemble of Alzheimer's amyloid-β peptide in aqueous solution and its implications for Aβ aggregation. *J. Mol. Biol.* 403, 148–165. doi: 10.1016/j.jmb.2010.08.003

von Bergen, M., Friedhoff, P., Biernat, J., Heberle, J., Mandelkow, E.-M., and Mandelkow, E. (2000). Assembly of tau protein into Alzheimer paired helical filaments depends on a local sequence motif (^{306}VQIVYK^{311}) forming β structure. *Proc. Natl. Acad. Sci. U.S.A.* 97, 5129–5134. doi: 10.1073/pnas.97.10.5129

Wälti, M. A., Orts, J., Vögeli, B., Campioni, S., and Riek, R. (2015). Solution NMR studies of recombinant Aβ(1-42): from the presence of a micellar entity to residual β-sheet structure in the soluble species. *Chembiochem* 16, 659–669. doi: 10.1002/cbic.201402595

Wälti, M. A., Ravotti, F., Arai, H., Glabe, C. G., Wall, J. S., Böckmann, A., et al. (2016). Atomic resolution structure of a disease-relevant Aβ(1-42) amyloid fibril. *Proc. Natl. Acad. Sci. U S A.* 113, E4976–E4984. doi: 10.1073/pnas.1600749113

Wang, Y., and Mandelkow, E. (2016). Tau in physiology and pathology. *Nat. Rev. Neurosci.* 17, 5–21. doi: 10.1038/nrn.2015.1

Weismiller, H. A., Murphy, R., Wei, G., Ma, B., Nussinov, R., and Margittai, M. (2018). Structural disorder in four-repeat tau fibrils reveals a new mechanism for barriers to cross-seeding of tau isoforms. *J. Biol. Chem.* 293, 17336–17348. doi: 10.1074/jbc.RA118.005316

Wille, H., and Requena, J. R. (2018). The structure of PrP^{Sc} prions. *Pathogens* 7:20. doi: 10.3390/pathogens7010020

Williams, A. D., Sega, M. D., Chen, M., Kheterpal, I., Geva, M., Berthelier, V., et al. (2005). Structural properties of Aβ protofibrils stabilized by a small molecule. *Proc. Natl. Acad. Sci. U S A.* 1002, 7151–7120. doi: 10.1073/pnas.0408582102

Xie, C., Soeda, Y., Shinzaki, Y., In, Y., Tomoo, K., Ihara, Y., et al. (2015). Identification of key aminoacids responsible for the distinct aggregation properties of microtubule-associated protein 2 and tau. *J. Neurochem.* 135, 19–26. doi: 10.1111/jnc.13228

Yong, W., Lomakin, A., Kirkitadze, M. D., Teplow, D. B., Chen, S. H., and Benedek, G. B. (2002). Structure determination of micelle-like intermediates in amyloid

β-protein fibril assembly by using small angle neutron scattering. *Proc. Natl. Acad. Sci. U S A.* 99, 150–154. doi: 10.1073/pnas.012584899

Yu, X., Luo, Y., Dinkel, P., Zheng, J., Wei, G., Margittai, M., et al. (2012). Cross-seeding and conformational selection between three- and four-repeat human tau proteins. *J. Biol. Chem.* 287, 14950–14959. doi: 10.1074/jbc.M112.340794

Zhang, W., Falcon, B., Murzin, A. G., Fan, J., Crowther, R. A., Goedert, M., et al. (2018). Heparin-induced tau filaments are polymorphic and differ from those in Alzheimer's and Pick's diseases. *bioRxiv* 8:e43584. doi: 10.1101/468892

Conflict of Interest Statement: The author declares that the research was conducted in the absence of any commercial or financial relationships that could be construed as a potential conflict of interest.